Dear Reviewer 1,

Thank you very much for identifying remaining issues in the manuscript.

We have now addressed your concerns and improved the manuscript accordingly. Please find attached as a *.pdf supplement our point-by-point reply; the labels in brackets refer to the position in the text.

Please let us know if you have further comments that need resolving.

Sincerely,
Ingo Sasgen & the REGINA team

Interactive comment on "Altimetry, gravimetry, GPS and viscoelastic modelling data for the joint inversion for glacial isostatic adjustment in Antarctica (ESA STSE Project REGINA)" by Ingo Sasgen et al.

Anonymous Referee #1

Received and published: 18 August 2017

Geodetic measurements in Antarctica measure a combination of Glacial Isostatic Ad-justment (GIA) and snow and ice thickness changes in Antarctica. Combination of the different data sets in an inversion approach might be the best method to isolate the dif-ferent components. Such inversion imposes requirements on the data sets. This paper presents analysis of data sets (altimetry, GPS, satellite gravity) and GIA model outputs to convert between the observables. The products can be used in an inversion to sep-arate the different components which is done in a separate study. However, the data sets can also be a useful resource for studies relying on one of the data sets. It is commendable that the authors have put great care in processing the data and making the results available. It will be a very useful resource for Antarctic mass balance studies. I reviewed an earlier version of the manuscript and I appreciate that comments from that review have been addressed in the current manuscript. There are in my opinion still several minor issues related to the description. The paper does not make sufficiently clear in the introduction what the processing adds to previous studies and what is re-quired of the data sets to be used in the inversion in paper II. Such explanation would guide the reader of this lengthy paper. Given that the main aim is to present 'data inputs', the descriptions of processing and errors is sometimes ambiguous. I hope the specific comments below help to improve this.

General comments:

The paper does not make sufficiently clear in the introduction what the processing adds to previous studies and what is re-quired of the data sets to be used in the inversion in paper II

We have added a description of the requirements imposed by the joint inversion. Moreover, we now describe the benefit of using response functions for the inversion at several places in the text. The processing of the data sets is not revolutionary, but the consistency and refinements achieved was only possible by the effort and discussions of the individual data providers engaged in the project.

Given that the main aim is to present ‘data inputs’, the descriptions of processing and errors is sometimes ambiguous

We have resolved issue of ambiguous processing and error descriptions, also raised by Reviewer 2.

Specific comments

74: the statement that forward models overpredict uplift rate measurements is not generally true, there are regional models that are tuned to the GPS data and there are instances where standard models underpredict observed uplift rates, see Wolstencroft et al (GJI 2015)

That is true. Another example of under-predicted GIA is the large uplift rates in the Amundsen Sea Embayment. We modified the statement. [R1_076]

102: How are the response functions used in combining them?

We added a clarifying text why the response functions are of advantage for solving the joint inversion problem based on the different input data (i.e. geophysical meaningful and Earth structure dependent ratio of the rate of geoid change / surface displacement, possible to use different filters on the input data sets). [R1_105]

Introduction: The introduction states that the data sets and modelling results are of value to address other research questions. But the paper itself does not yet contain a research question. In addition, it is not clear form the introduction why the processing is better than previous analysis of the data sets. For example, would you expect improve-ment compared to Thomas et al. (2011) or are differences merely ‘small processing strategy changes’ (line 272).

We specified the most important advancement in the processing of each data set [R1_099].

It should also be summarized what requirements the in-version poses on the data and kernels, for example in terms of time period, resolution, error (= weight in the inversion). Such explanation would help the reader evaluate the (many) choices that are made in the manuscript.

We spelled out the requirements necessary for the joint inversion [R1_111]

121 and further. More information is given on the corrections, which is helpful, but not yet what the error in the corrections is (or if it is insignificant) and if it is added to the height error.

We did not evaluate the uncertainties caused by variations in the processing choices. This is now stated in the text [R1_157].

> 138: 'residual uncertainties' is confusing as it sounds like the residual of the uncertainties? In any case it does not correspond to equation 1, which gives non-dimensional values as both e and x have the same unit. Also, it should be discussed why residuals are a good approximation for errors.

We reformulated the term "residual uncertainties". We referred the reader to Eq. 1 in Hurkmans et al. 2012, who provides a detailed description of the error estimation. And we explained why residuals are used as part of the uncertainty estimate [R1_168].

> 160: 'the standard deviations of the rates'. Are they also calculated according to equation 1?

Yes. We included a reference to Eq. 1.

> 208: Errors could be important in the inversion to weigh the contribution from the different data sources. Neglecting model uncertainties because estimates are not available is not really a satisfactory solution.

We agree that the uncertainties should in principle be considered. But they will be small, such that the current estimate of elevation rate uncertainties captures the dominant sources. We added explanatory sentences [R1_243]

> 243: This is the first time this data set is mentioned. Does it include error estimates?

Yes, we added this data set for completeness, although it is discussed in Sasgen et al. 2017. We do not provide uncertainties with it [R1_284].

> 339: Do you have any explanation for the difference?

Currently, this difference is unexplained. A step-by-step intercomparison of the GPS processing with Wolstencroft et al. 2015 beyond the scope of this paper. We added the sentence "The systematic differences between Wolstencroft et al. (2015) and the REGINA values for Palmer Land are currently unexplained and a matter of ongoing investigations" [R1_370]

> 361: What is the threshold and how did you weigh the average? This manuscript present data sets and their analysis so the procedure should be clear.

We added the thresholds for the clustering, and specified that weighted averaging was done for the positions. [R1_361]

> 470: it is not clear what is meant. Is the search range for the parameters limited? Is the range of m limited to values higher than 10?

We added clarifying text. [R1_470].

471: 476 and further, it is confusing to use both interannual and non-linear because they can seem the same but are not necessarily so.

We now consistently use “non-linear” now instead of “interannual”. The positions in the text are marked [R1_476].

404 “zero difference”: better to write a full sentence here.

We added a full sentence. [R1_404]

495: “the post-fit RMS residual for this known temporal signal variation”. This is not clear. In line 449 the residual is defined as GRACE minus ice elevation, fitting is not mentioned. figure 5: the axis label states ‘linear trend residuals’, but the text in page 503 states that also annual oscillations are removed. Please make the descriptions consistent.

We changed the labeling and caption of Fig. 5. And, added clarifying text. The optimization of the filter parameters is done on GRACE rates minus ice elevation rates. The SMB reduction is intended to reduce multi-year fluctuations, for improving the residual GRACE uncertainty – i.e. to see whether the residual uncertainty gets closer to the nominal calibrated uncertainty of the GRACE coefficients. The de.trending of step 3 includes a annual oscillation to account for remaining seasonal variations of SMB not captured by the SMB model. The seasonal is not important and could be neglected for this analysis yielding the similar results [R1_495].

509 and further. The procedure seems OK but the reasoning does not make sense. if you downweigh months with high post-fit RMS the post-fit RMS decreases. That seems to me a mathematical certainty and in that case it should not be used to say that the downweighting is beneficial.

Accepted. The second half of the sentence was removed. [R1_509]

514: What is meant by more accurate? A higher RMS when you include noisier months is still an accurate representation of the noise.

We changed the wording [R1_514].

Section 4: it is not clear to me what is done with the signal corruption due to Swenson and Gaussian filtering. Is that added to the error? Or will the filtering be applied to the other datasets in the inversion? Line 924 states that there is no magnitude bias (in the geoid rate?), but that would suggest that filtering is not really necessary

The signal corruption itself is not considered as a component of the uncertainty estimate. It is arguable, whether the Swenson filtering should be applied to the altimetry data before the joint inversion, as this data set has a different error structure. The largest effect is due to the signal loss caused by the smoothing with a Gaussian filter. This is considered by applying the Gaussian smoothing to the altimetry data set and the viscoelastic response functions. We added more explanatory text [R1_511].

594: it would help the reader to be more clear about why you need the response kernels in the inversion. Only in the conclusions on line 846 it is mentioned that you need the kernels for ratio of gravity and displacement.

We added explanations in the introduction [see R1_105]. We also added more explanation in Section 5 [R1_653].

631: Does the range span the values in the Priestley and McKenzie 3D viscosity model that you use later?

Yes, the range is guided by the model of Priestley & McKenzie (2013). We added a sentence. [R1_696]

645: 10ˆ22 is quite low to be considered fully elastic. Such viscosity would still give noticeable response from ice load changes since the last glacial maximum.

We agree. However, the value has to be considered as a threshold value to map the continuous viscoelastic parameter in Priestley & McKenzie (2013) obtained by Earth modelling to our layered model for the calculating the viscoelastic relaxation. The effect of changing this parameters was presented in Sasgen et al. 2017 (Fig. S4). Explanation was added. [R1_712].

657: make clear that it is the standardized ratio (i.e. it starts at 1)

Clarified [R1_700].

658: according to appendix A.6 it should be 1/eˆ2

Corrected [R1_700].

section 5.5: another assumption(mentioned in the appendix in line 932) is that the equilibrium has been reached. If load changes constantly, then at present you are not in a state of equilibrium with constant displacement rate. This is mentioned later but could also be added here. Another assumption is that upper and lower mantle viscosity are assumed known.

We agree. We added these assumptions to the list [R1_795].

733: e-dot was used for geoid rate in line 673

We unified the nomenclature.

842: The response functions in the paper are produced for a continuously changing load. It is not yet possible to draw conclusions about the exact timing of the load from that.
843:

Added a sentence on this limitation [R1_921]

846: the ratio should be for rates, not the gravity disturbance itself.

Agreed. Added “rates of”. [R1_923].

848 and further: this is an important justification that should be mentioned in the introduction as well

We added the justification to the Introduction and to the Section 5.

935: and on elastic parameters and density

Typos etc

81: grammar ‘And thus to’

Corrected.

95: grammar, change ‘invasion’

Corrected.

115: I suggest adding this to the acknowledgements instead

Moved to the acknowledgements.

150: ‘the’ before ICESAT

Inserted ‘the’.

figure 1: when zooming in I see many different colors. That might be the result of lower resolution picture, but it makes it hard to interpret the colors described in the caption

This seems to be a resolution problem. We will make sure this is ok in the final digital version.

caption figure 2: space before sigma

Inserted space.

213: should it be 20 km grid?

The grid resolutions as stated are correct.

219: typo? something wrong with the degree symbol here and further on

Corrected degree symbols.

228: abbreviation should be introduced

FDM is now spelled out “firn-densification model”.

229: typo?

Corrected.

246: kg/m^3 instead of km/m^3

Very true. Thank you.

302: can refer to section 3.2.2 caption

Table 4: “Table Appendix A.4”

Reference included

370: provide link?

CS

Resolved missing link.

533: expanded ‘to’

Inserted ‘to’

593: remove ‘a’

Removed.

601: add ‘are’ before ‘a classic’

Included ‘is’

648: considered

Corrected.

649: parameter

Changed to singular.

801: compositing?

Removed.

807: terms

Corrected.

813: change ‘over’ to ‘about’

Changed.

834: ‘however’ implies a contradiction, I don’t see

Removed.

table A.2, better to write approx in full.

Changed.

figure A.4 and text use both mm/a and m/year

Changed.

figure A.5 axis label: standardized

Labels unified.

Altimetry, gravimetry, GPS and viscoelastic modelling data for the joint inversion for glacial isostatic adjustment in Antarctica (ESA STSE Project REGINA)

Ingo Sasgen[1], Alba Martín-Español[2], Alexander Horvath[3], Volker Klemann[4], Elizabeth J. Petrie[5], Bert Wouters[6], Martin Horwath[7], Roland Pail[3], Jonathan L. Bamber[2], Peter J. Clarke[8], Hannes Konrad[9], Terry Wilson[10] and Mark R. Drinkwater[11]

1. Division of Climate Sciences, Alfred Wegener Institute, Bussestraße 24, 27570 Bremerhaven, Germany.
2. School of Geographical Sciences, University of Bristol, University Road, Clifton, Bristol BS8 1SS, United Kingdom.
3. Institut für Astronomische und Physikalische Geodäsie, Technische Universität München, Arcisstraße 21, 80333 München, Germany.
4. Department of Geodesy, GFZ German Research Centre for Geosciences, Telegrafenberg, 14473 Potsdam, Germany.
5. School of Geographical and Earth Sciences, University of Glasgow, Glasgow, G12 8QQ, United Kingdom.
6. Institute for Marine and Atmospheric Research, Utrecht University, Princetonplein 5, 3584 CC, Utrecht, The Netherlands.
7. Institut für Planetare Geodäsie, Technische Universität Dresden, Helmholtzstr. 10, 01069 Dresden, Germany.
8. School of Civil Engineering and Geosciences, Newcastle University, Newcastle, NE1 7RU, United Kingdom.

9. School of Earth and Environment, University of Leeds, Leeds, LS2 9JT, United Kingdom.
10. School of Earth Science, Ohio State University, 275 Mendenhall Lab, 125 South Oval Mall, Columbus OH, 43210, USA.
11. Mission Science Division, European Space Agency, European Space Research and Technology Centre, Keplerlaan 1, Noordwijk 2201 AZ, The Netherlands.

Keywords:

Global change from geodesy, Gravity anomalies and Earth structure, Loading of the Earth, Glaciology, Antarctica, Joint inversion

ABSTRACT

[R2_036] The poorly known correction for the ongoing deformation of the solid Earth caused by glacial isostatic adjustment (GIA), is a~~A~~ major uncertainty in determining the mass balance of the Antarctic ice sheet from measurements of satellite gravimetry, and to a lesser extent satellite altimetry~~, is the poorly known correction for the ongoing deformation of the solid Earth caused by glacial isostatic adjustment (GIA)~~. In the past decade, much progress has been made in consistently modelling ~~the~~ ice sheet and solid Earth interactions; however, forward-modelling solutions of GIA in Antarctica remain uncertain due to the sparsity of constraints on the ice sheet evolution, as well as the Earth's rheological properties. An alternative approach towards estimating GIA is the joint inversion of multiple satellite data – namely, satellite gravimetry, satellite altimetry and GPS, which reflect, with different sensitivities, trends of recent glacial changes and GIA. Crucial to the success of this approach is the accuracy of the space-geodetic data sets. Here, we present reprocessed rates of surface-ice elevation change (Envisat/ICESat; 2003-2009), gravity field change (GRACE; 2003-2009) and bedrock uplift (GPS; 1995-2013.7). The data analysis is complemented by the forward-modelling of viscoelastic response functions to disc load forcing, allowing us to relate GIA-induced surface displacements with gravity changes for different rheological parameters of the solid Earth. The data and modelling results presented here are available in the Pangaea; https://doi.pangaea.de/10.1594/PANGAEA.875745. The data sets are the input streams for the joint inversion estimate of present-day ice-mass change and GIA, focusing on Antarctica. However, the methods, code and data provided in this paper are applicable to solve other problems, such as volume balances of the Antarctic ice sheet, or to other geographical regions, in the case of the viscoelastic response functions. This paper presents the first of two

contributions summarizing the work carried out within a European Space Agency funded study, REGINA.

1. Introduction

[R2_066] Glacial isostatic adjustment (GIA), the viscoelastic deformation of the solid Earth in response to climate-driven ice and water mass redistribution on its surface, is poorly constrained in Antarctica. The primary reason is the sparseness of geological evidence ~~of~~ for the past ice sheet geometry and local relative sea-level change. These are important constraints on the exerted glacial forcing and on the viscoelastic structure of the lithosphere and of the mantle~~, respectively~~, which ~~concertedly~~ together determine the signature of GIA (e.g. Peltier, 2004; Ivins and James 2005; Whitehouse et al. 2012: van der Wal et al., 2015). The predictions of GIA in Antarctica remain ambiguous (Shepherd et al. 2012, suppl.) and cause a large uncertainty in gravimetric mass balance estimates of the ice sheet of the order of the estimate itself (Martín-Español et al. 2016b). Measurements of bedrock uplift by GPS ~~have shown to be~~ are inconsistent with the predictions of existing GIA. [R1_076] In many regions, uplift rates and thus mass increase due to GIA is over-predicted (Bevis et al. 2009), biasing estimates of present-day Antarctic ice-mass loss from GRACE to more negative values. However, for regions with a weak Earth structure, large uplift signals are recorded by GPS (e.g. Groh et al. 2012), which are likely caused by load changes within the past few thousand year, and often not accurately represented in GIA predictions (Wolstencroft et al. 2015).

Much progress has been made in reconstructing the ice sheet evolution from geomorphological evidence (Bentley et al. 2014) and inferring the underlying Earth structure from seismic observations (An et al. 2015; Heeszel et al. 2016). However, an independent approach to constraining GIA is to make use of the different sensitivities of the various types of satellite data to recent glacial changes and GIA, respectively. ~~And thus to separate~~ Separating both signals in a joint inversion approach has been pursued by e.g. Wahr et al. 2000; Riva et al.

2009; Wu et al. 2010; Gunter et al. 2014, Martín-Español et al. 2016a. Another approach used regional patterns of GIA from forward modelling and adjusted them to GIA uplift rates in Antarctica (Sasgen et al. 2013).

In this paper, we present methods and data inputs in preparation of solving the joint inversion problem for GIA in Antarctica. As the GIA process is gradual, causing an approximately constant rate of change within a decade, we first process the satellite data to recover optimal temporal linear trends. [R2_020] We focus on the trends derived for the time period 2003-2009 in which GRACE and ICESat operated simultaneously. Note that the stationarity of the trend is a key assumption underlying our approach, when including GPS rates covering a longer time span (1995-2013.7)~~.~~ However, limiting the GPS data to the time span 2003-2009 leads to a significant reduction of the number of stations for which reliable trends can be estimated, and, hence, a loss of spatial coverage. For comparison, the reader is advised to the data archive, in which GPS uplift rates for the time periods 2003-2009 and 2003-2013.7 are made available.

[R1_099] In this paper, we present refined ~~We refine existing~~ procedures for estimating trends ~~for~~ of the data sets on surface-ice elevation changes, surface displacement and gravity field changes. The rates of surface-ice elevation change~~s~~ from Envisat and ICESat satellite altimetry are improved by ~~(Section 2), by~~ combining both data sets based on their respective uncertainties, increasing the spatial coverage and accuracy of the elevation rates (Section 2). ~~;~~ ~~bedrock~~ Bedrock displacement ~~–~~from *in situ* networks of GPS stations in Antarctica are improved in coverage by allowing for campaign-based data and carefully assessing the uncertainty of the trend with a noise model (Section 3). Compared to the rates in Thomas et al. (2011) also more stations and longer time series are included~~,~~ ~~and~~ The gravity field changes from GRACE are refined compared to previous work by optimizing the de-striping filtering for the region of Antarctica (Section 4). [R1_111] The processing aims at fulfilling the requirement of the joint inversion to combine input data based on the same time period (not possible for GPS without having to ignore a large number of stations) and covering entire Antarctica, accompanied by a realistic description of the uncertainties.

We also present forward modelling results of viscoelastic response functions to disc load forcing for the range of Earth structures likely to prevail in Antarctica (Section 5). [R1_105] The viscoelastic response functions allow us to combine the surface displacement and gravity changes based on the physical description of the Earth's viscoelastic response for a specified Earth structure. In addition, the response functions enable us to combine data sets of different spatial resolutions, as this is the case for GPS, GRACE and altimetry.

The determination of viscoelastic response functions is a classic topic in solid Earth modelling (e.g. Peltier & Andrews, 1976), though uncommon in the application to joint ~~invasion~~ inversion studies of satellite data. Although this paper focusses on Antarctica, the response functions and data processing techniques presented here are applicable to other regions. The response kernels represent a wide range of Earth structures and can be used for the separation of superimposed present-day (elastic) and past (viscoelastic) signatures of mass change in other regions with a similar Earth, for example hydrological storage changes and GIA in North America and Alaska. The response functions give insight into the temporal and spatial scales of deformation expected for Antarctica, and are crucial when combining the input data streams.

The data sets and modelling results presented in this paper are accessible in the Pangeae archive, https://doi.pangaea.de/10.1594/PANGAEA.87574 – subsections provide user guidance and point to data and code stored in the archive. As mentioned above, the data sets and modelling results are of value to address other research questions as well. For example, the GPS rates provided are useful for the validation of forward modelling GIA solutions, the GRACE gravity rates can be used for mass balance studies, and altimetry data 2003-2009 can be extended with the ongoing CryoSat-2 mission to infer volumetric mass balances, also over the ice shelves. The viscoelastic response functions are based on Earth model parameters potentially suitable to other geographical regions, as well; they are useful for similar studies combining different data sets of geodetic observables, surface deformation, gravity field change, and topographic change in glaciated areas.

The actual method of the joint inversion is described in a second contribution of the REGINA project team (Sasgen et al. submitted2017). In this second paper, the resulting GIA estimate is also compared to previous studies. The processing of the data issued here was enabled by the European Space Agency within the CryoSat+ Support To Science Element Study REGINA.

2. ALTIMETRY DATA ANALYSIS

2.1 *ICESat elevation rate determination*

We use along-track altimetry measurements from *ICESat 633 Level 2*, providing high-resolution elevation change observations for the period February 2003 until October 2009. Two corrections are applied to this data set: the range determination from Transmit-Pulse Reference-Point Selection (Centroid vs. Gaussian) (Borsa et al. 2014) available from the National Snow and Ice Data Center (NSIDC), and the inter-campaign correction (Hofton et al. 2013). The Centroid-Gaussian correction is a well-established correction and has been incorporated to the latest ICESat release (634). Concerning the ICESat Intercampaign Bias (ICB) correction, uncertainties are available at Hofton et al (2013). Furthermore, several studies have determined this correction from different methodologies. For a summary of published ICESat ICB corrections see Scambos & Shumman (2016). [R1_157] Note that these corrections are part of a widely accepted procedure and their effect on the elevation rates and uncertainties caused by varying the processing choices have not been evaluated. Because the ICESat tracks do not usually overlap, a regression approach is used in which topographic slope (both across-track and along-track) and the rate of surface-elevation change $\boldsymbol{y}^{h}_{\mathrm{ICESat}}$, are simultaneously estimated using the 'plane' method (Howat et al. 2008~~'~~) over areas spanning 700 m long and few hundred meters wide. A regression is only performed if a plane has at least 10 points from four different tracks that span at least one year. Regression was carried out twice; first, individual elevation measurements with corresponding residuals outside the range of two standard deviations were detected, then, the regression was repeated omitting these outliers. The standard deviation of the regression coefficient, here taken as the uncertainty of the elevation rate, σ^{h}(here, ICESat) is calculated by the propagation of the [R1_168] residuals of the ~~uncertainties of the~~ input data and the estimated topographic heights,

$$\hat{s}_{\text{ICESat}} = \sqrt{\frac{\sum e_i^2 / (n-2)}{\sum (x_i - \bar{x})^2}}, \quad (1)$$

to the trend parameter (see Eq. 1 in Hurkmans et al. 2012), where $\boldsymbol{e}$ is the vector of residuals, n is the sample size ($i = 1,2, \dots, n$), and $\boldsymbol{x}$ is the vector of input elevations with mean $\bar{\boldsymbol{x}}$. This standard deviation (σ_{ICESat}) takes into account the sample size and the variance of both input data and residuals of the regression (Hurkmans et al. 2012). The residuals of the regression are used as they quantify the approximation of fitting the data with a plane. The exact ICESat observation periods are shown in the Appendix (A.1, Table A.1). Then, the elevation rate and its uncertainty are interpolated (bi-linear) [R2_156] to a common 10×10 km grid in polar-stereographic projection (central latitude 71°S; central longitude 0°W, and origin at the South Pole, WGS-84 reference ellipsoid).

2.2 *Envisat elevation rate determination*

We use a time series of elevation changes derived from along-track Envisat radar altimetry data for the interval January 2003 to October 2009 (coeval to ICESat time span). Elevation rates y^h_{Envisat} are obtained at points every 1 km along track, by binning all the echoes within a 500 m radius. Then, a 10-parameter least squares model is fitted in order to correct for the across-track topography and changes in snowpack properties. The least square model is defined in Flament and Remy (2012). The estimated parameters include parameters determined for the backscatter, leading-edge width and tailing-edge slope, the mean altitude, quadratic surface slope parameters to define surface curvature and a linear time trend. A digital elevation model was not used for the correction of the topographic slope. For processing reasons, the temporal resolution is re-sampled from 35 days to monthly periods for each grid cell, before estimating the elevation rates. This has a minor effect on the elevation rate estimate ([R2_169] smaller than ± 1 cm/yr) and reduces the standard deviation by about 14 %. As ~~for~~ with ICESat, the elevation rate is interpolated to~~-~~a common 10×10 km polar stereographic grid (and 20×20 km for download in the archive [R2_172])~~,~~ and the standard deviations of the rates within each grid cell are taken as an estimate of the measurement uncertainty, σ_{Envisat} according to Eq. 1~~.~~

2.3 *Combination of Envisat and ICESat*

We produce a combined rate of surface-elevation change product from the ICESat and Envisat datasets for the Antarctic ice sheet, y^h. The aim is to take advantage of the high spatial resolution of ICESat data and the high temporal resolution and high-track density of the Envisat data.

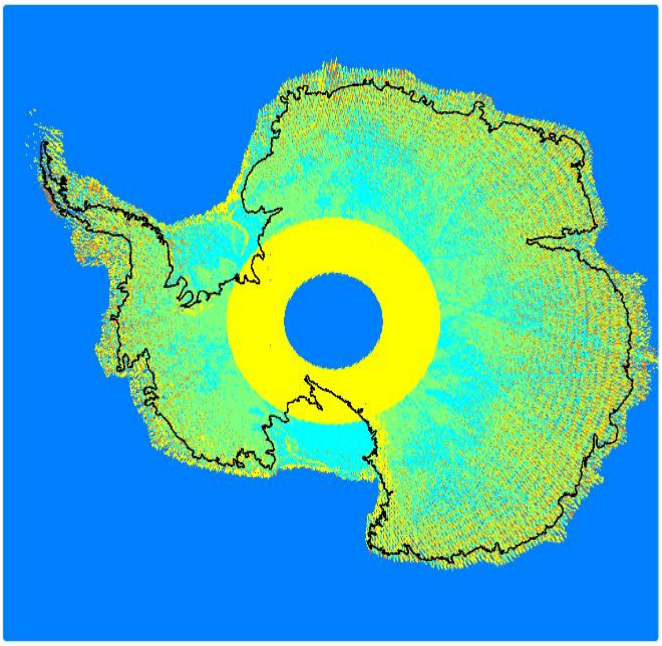

Figure 1. Mask for the combination of Envisat/ICESat. ICESat but not Envisat available (yellow), $\sigma_{ICESat} \leq \sigma_{Envisat}$ (green), $\sigma_{ICESat} > \sigma_{Envisat}$ (turquoise), Envisat but not ICESat available (orange), and no data (blue). No interpolation is used.

We combine the two altimetry datasets based on their common 10×10 km polar-stereographic grid. At each location, the elevation rate with the smallest standard deviation is chosen from either Envisat or ICESat datasets. [R2_181] We prefer this masking procedure instead of a weighted average, in order to avoid introducing possible biases associated with gridded elevation rates of very high uncertainty.

Fig. 1 shows the resulting mask underlying the combination. It is evident that some grid points are only represented by either ICESat or Envisat. Most prominent is the narrowing of the polar gap with ICESat data, resulting from the 81.5°S latitude limit for Envisat compared to 86°S for ICESat due to satellite orbit inclination. On the Antarctic Peninsula, Envisat picks up some points that are not present due to a sparser track coverage in the ICESat data set. As expected, ICESat outperforms Envisat in terms of uncertainty of the elevation rate over steep topographic slopes and along the ice sheet margins. This is due to the smaller footprint of the laser altimeter, its higher accuracy and lower slope-dependent uncertainty (e.g. Brenner 2007). On some flat areas and over some faulty ground tracks, where ICESat data measurements are scarce, however, Envisat provides better temporal and spatial coverage leading to better accuracy of the resulting elevation rates. The resulting combined data set of surface-elevation rates and its uncertainties are shown in Fig. 2.

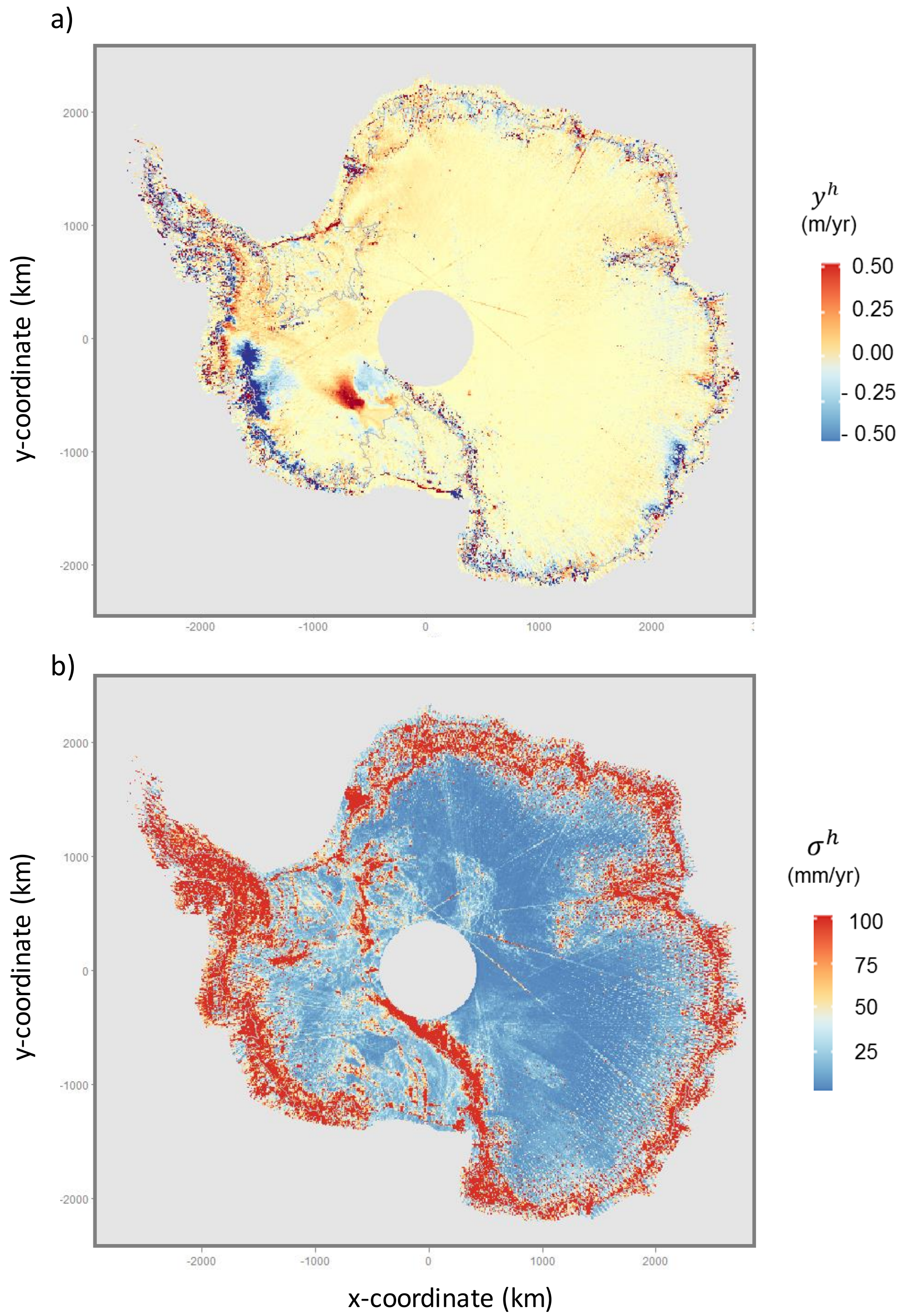

Figure 2: a) Rate of surface-ice elevation change y_h and b) associated uncertainties σ_h derived from Envisat/ICESat combined dataset for the time interval 2003-2009. No interpolation is used; grid points without values are empty (shaded grey).

2.4 *Firn correction*

The elevation rates derived from ICESat and Envisat are corrected for changes in the firn layer thickness using the firn compaction model of Ligtenberg (2011), which is driven by the regional atmosphere and climate model RACMO2/ANT (Lenaerts, 2010). We determine the firn compaction for January 2003 to October 2009, with respect to the mean of the years 1979 to 2002 and estimate a temporal linear trend, h_{comp}. The model output is re-gridded onto the 10×10 km common grid using nearest neighbor interpolation. The standard deviation of the re-gridding is less than 1 cm/yr, causing a maximum change of 2 % of the firn compaction rate. Note that the firn compaction model has a spatial resolution of 27 km, potentially neglecting finer-scale processes relevant for the altimetry data. Clearly, the re-gridding uncertainty stated above is merely a minimum estimate, neglecting, for example, uncertainties in the calibration or the atmospheric forcing of the firn compaction model.

The data were re-sampled from every two days to monthly mean time periods for every grid cell before estimating elevation rates. As ~~for~~ with the Envisat and ICESat data, no seasonal terms ~~are~~ were co-estimated and removed (i.e. annual and semi-annual). We do not apply an *a priori* correction for surface-mass balance (SMB) trends, in accordance with the GRACE processing (Section 5), which requires defining a climatological reference period. Note that applying the commonly used reference period (1979 to present) leads to spurious accumulation anomalies in the altimetry data (see Appendix A.2, Fig. A.1). The derivation of an adequate climatological reference epoch in the RACMO2/ANT simulations is in itself challenging and beyond the scope of this paper.

The total uncertainty of the rate of elevation change from satellite altimetry is calculated by

$$\sigma_h = \sqrt{\sigma^2_{Envisat/ICESat} + \sigma^2_{Firn}}\ , (2)$$

where the standard deviation of the firn correction, σ_{Firn} is the formal regression uncertainty (neglecting model uncertainties, as these are not available), and we assume the error sources to be uncorrelated. [R1_243] It is recognized that neglecting uncertainties of the firn model leads to underestimated values of σ_h. However, the magnitude of the firn correction itself is small (see Appendix A.2) compared to the observational uncertainties, and the associated underestimation of σ_h is likely to be small.

2.5 *Data availability*

Annual elevation trends from a combination of Envisat and ICESat data are provided for the time period between February 2003 and October 2009. Trends have been corrected for firn densification processes using RACMO2/ANT. Elevation trends are provided in a 20 km polar stereographic grid (central meridian 0◦ , standard parallel 71◦ S) with respect to the WGS84 geoid. X and Y are given in km, and the elevation rate and its standard deviation are given in m/yr.

The altimetry data and related ancillary data are directly accessible in the Pangaea repository: [R2_010]

http://hs.pangaea.de/model/Sasgen-etal_2017/Ice_sheet_topographic_change.zip

2.5.1 *ICESat elevation trend for the* time period between February 2003 and October 2009.

The dataset is provided in a 10 km grid in polar stereographic projection (central meridian 0◦da standard parallel 71◦ S) with respect to the WGS84 geoid. X and Y are given in km, and the elevation rate and its standard deviation are given in m/yr.

2.5.2 *Envisat elevation trend for the time period between February 2003 and October 2009.*

The dataset is provided in a 10 km grid in polar stereographic projection (central meridian 0∘ , standard parallel 71∘ S) with respect to the WGS84 geoid. X and Y are given in km, and the elevation rate and its standard deviation are given in m/yr.

2.5.3 ICESat & Envisat combination for time period between February 2003 and October 2009.

Elevation changes have been corrected for firn densification processes using a ~~FDM~~firn-densification model. The dataset is provided in a 10 km grid in polar stereographic projection (central meridian 0°,∘~~f∘~~ standard parallel 71°~~∘~~ S) with respect to the WGS84 geoid. X and Y are given in km, and the elevation rate and its standard deviation are given in m/yr.

2.5.4 *Annual elevation trends from CryoSat-2 derived from a single trend covering the time period 2010-2013.*

An acceleration term in areas with dynamic thinning was added to the linear trend to obtain annual rates. Elevation trends are provided at 10 km resolution in a polar stereographic grid (central meridian 0°~~∘~~ , standard parallel 71°~~∘~~ S) with respect to the WGS84 geoid. X and Y are given in km and the elevation rate and its standard deviation are given in m/yr.

2.5.5 *Elevation changes from firn model*

Annual firn densification rates over 2003-2013 rates obtained from RACMO2.3. Data is provided in a 27 km polar stereographic grid (central meridian 0∘ , standard parallel 71∘ S) with respect to the WGS84 geoid. X and Y are given in km and the annual firn densification rates in m/yr.

2.5.6 *Snow / ice density map*

[R1_284] To perform the conversion of volume change to mass change, a ~~The density map for volume-to-mass conversion is~~ density map is provided in 20 km resolution in a polar stereographic grid (central meridian 0°~~°~~, standard parallel 71°~~°~~S) with respect to the WGS84 geoid. X and Y are given in km and density in k~~gm~~/m³. We provide the data set at this point for completeness; more details on the generation of this density map is given in Sasgen et al. (2017).

2.5.7 *ICESat/Envisat combination mask*

Mask used for combining ICESat and Envisat in a 10 km resolution and polar stereographic coordinates.

X and Y are coordinates in km and the id represents whether ICESat or Envisat has been used to construct the elevation change combination.

4: only Envisat was available

3: only ICESat was available

2: ICESat lower errors

1: Envisat lower errors

3. GPS UPLIFT RATE ESTIMATION & CLUSTERING

The aim of the GPS time series analysis is to derive uplift rates, y_u that represent the ~~geophysical~~ vertical ground motion at the sites as accurately and robustly as possible. We derive uplift rates based on GPS records from a total of 118 Antarctic sites. Data were processed from 1995 day of year (doy) 002 to 2013 doy 257 (1995.0-2013.7) but data at individual sites are of varying length and quality. The processing and uplift rate and uncertainty estimation methodology are documented in detail in Petrie et al. (in prep. a, b), but a short summary is given here for convenience. It resembles that of Thomas et al. (2011), but with more recent processing software (GIPSY 6.2) and model updates (including second order ionospheric and earth radiation models): an initial satellite orbit and clock estimation step is performed, using a carefully selected balanced stable global network of GPS sites (at the time of processing JPL reprocessed orbits for these state-of-the-art options were not available) [R2_279]. The orbits and clocks are then used to perform precise point positioning (PPP) processing of all the available Antarctic sites of interest. A mini-ensemble was created to investigate systematic processing uncertainties and manual investigation was performed of the effects of possible systematic errors in the time series on uplift rates. The mini-ensemble investigation showed that decisions taken when analyzing time series tended to have larger effects on uplift rates and uncertainties than the effects of small processing strategy changes. Outliers and systematic errors, such as offsets due to equipment changes or other causes, were removed where possible. Due to the varying characteristics of the time series it was not possible to use the same approach at all sites. The strategy was as follows (and is summarized in Appendix A.3, Fig. A.3). For sites with over 2000 days of data, uplift rates and associated uncertainties were estimated using the CATS software (Williams 2008). We co-estimated a white-noise scale factor for the formal uncertainties, and a power-law noise amplitude with the index fixed to -1 (flicker noise), along with the temporal linear trend (rate), seasonal (annual and semi-annual) parameters, and sizes of the offsets (at the specified epochs).

The median values of the white-noise scale (1.6) factor and the power law noise amplitude (13.4 mm),[R2_295] derived from these long time series, were then used to propagate rates and uncertainties for the shorter time series, for which CATS cannot produce reliable estimates of the error model. For the propagation, the time series with fewer than 2000 epochs are additionally subdivided into two categories; continuous sites (≥ 2.5 yr), for which periodic parameters are estimated in the propagation of uncertainties, and very short continuous sites (< 2.5 yr) and campaign sites for which periodic parameters are not estimated. For each campaign, 1 mm of noise was added when propagating the uncertainties, to allow for tiny differences when re-setting up equipment.

Finally, for each site, the uplift rate y^u and its uncertainty σ^u are assessed by manually removing portions of the time series (for example deleting campaigns in turn). If the rate changes by an amount larger than the propagated uncertainty for the site, the uncertainty is assigned as ± the maximum difference in rate, and the rate is adjusted, if necessary, to the values of the most likely part of the range. Sites with only two campaigns were assigned an uncertainty of ± 100 mm/yr, unless there was further evidence for or against the existence of systematic errors.

Table 1 summarizes the rate estimation methods and the number of sites for each. For further details and full information on individual rates and time series, see Petrie et al. (in prep a) for a full description of the processing and ensemble evaluation, and Petrie et al. (in prep b) for details of time series analysis and rate and uncertainty estimation. ~~Table 1 shows the numbers of sites at which each approach was taken.~~ Further work was undertaken to combine or 'cluster' the rates regionally for inclusion in the estimation process – see the REGINA Paper II (Sasgen et al. 2017), Section 3.2.2 ~~for details~~and Table Appendix A.4 for more details.

Table 1: Number of sites for each GPS uplift rate and uncertainty estimation method.

Rate and uncertainty estimation method	Number of sites (118 total)
CATS rate and uncertainty (‘cats, cats’)	18
CATS rate, manually increased uncertainty (‘cats, eman’)	2
Propagated rate and uncertainty (‘prop, prop’)	28
Propagated rate and manually increased uncertainty (‘prop, eman’)	50
Manually adjusted rate and manually increased uncertainty (‘rman, eman’)	20

Table 2. Uplift rates y^u and associated uncertainties σ^u (mm/yr) for selected GPS sites with more than 2000 epochs of data, compared to data published by Thomas et al. (2011) and Argus et al. (2014). Temporal components and noise characteristics are derived using the CATS software (Williams 2008), i.e. ‘cats, cats’ method.

Site	REGINA		Thomas et al. (2011)		Argus et al. (2014)	
	y^u	σ^u	y^u	σ^u	y^u	σ^u
cas1	**1.5**	0.2	**1.2**	0.4	**1.7**	0.8
crar	**0.7**	0.4	**1.0**	0.7	**1.0**	0.6
dum1	**-0.3**	0.3	**-0.8**	0.5	**–0.2**	0.8
maw1	**-0.4**	0.2	**0.1**	0.4	**0.2**	0.6
mcm4	**0.8**	0.2	**0.7**	0.4		
sctb	**0.9**	0.5	**0.6**	1.1		
syog	**1.1**	0.2	**2.3**	0.4	**0.6**	0.8
tnb1	**0.1**	0.5	**-0.2**	0.8	**–0.4**	1.0
vesl	**0.4**	0.3	**1.1**	0.5	**1.5**	0.8
McMurdo*					**1.0**	0.6

*Sites: crar-sctb-mcm4-mcmd

Comparison with existing results

Next, we briefly compare the uplift rates at individual sites (data span 1995.0-2013.7) derived from the GPS processing described above with those available from three previous studies: Thomas et al. (2011) (data span 1995.0-2011.0), Argus et al. (2014) (data span 1994-2012) and the more geographically limited set of Wolstencroft et al. (2015) (data span 2006-late 2013, focused on Palmer Land). It should be noted that the REGINA and Wolstencroft et al. (2015) rates are in ITRF2008, the Thomas et al. (2011) rates are in ITRF2005 (which has negligible scale or translation differences to ITRF2008), and the Argus et al. (2014) rates are in a reference frame specific to the paper which they note yields 0.5 mm/yr more uplift than ITRF2008 at high southern latitudes. All rates from Argus et al. (2014) in Tables 2, 3 and 4 are shown as given in the original paper. [R2_327].

Due to the large number of Antarctic sites, in total 118, we focus the comparison on the uplift rates and uncertainties derived by the methods 'cats, cats' (Table 2) and 'prop, prop' (Table 3). Uplift rates resulting from our study are provided in Appendix A.4 for all sites (Table A.2). Tables A.3 shows comparisons with the values of Thomas et al. (2011) and Argus et al. (2014) for 'prop, eman' sites not shown in the main text. All uplift rates, y^u , are in mm/yr, with uncertainties reflecting 1-sigma standard deviations, σ^u. Sites with particularly complex non-linear time series such as those at O'Higgins (ohi2, ohig) and Palmer (palm) in the Antarctic Peninsula are omitted here, as comparison with different studies is potentially misleading due to the effects of different measurement time periods. Table 2 shows data for selected sites with

Table 3. Uplift rates y^u and associated uncertainties σ^u (mm/yr) for selected GPS sites with fewer than 2000 epochs for data, compared to data published by Thomas et al. (2011) and Argus et al. (2014). Noise characteristics are derived median values from CATS software results for longer station records and propagated in the parameter estimation ('prop, prop' method). See Appendix A.4, Table A.2 for a full list of rates from this study.

Site	REGINA		Thomas et al. (2011)		Argus et al. (2014)	
	y^u	σ^u	y^u	σ^u	y^u	σ^u
belg	**-1.4**	0.7	**3.0**	1.5	**0.8**	2.4
dupt	**11.5**	1.1			**12.4**	2.5
fonp	**13.5**	1.8			**14.8**	3.4
frei	**-4.4**	0.7			**–2.9**	1.4
hugo	**0.9**	1.3			**1.7**	3.6
robi	**8.7**	1.5			**8.7**	3.2
roth	**5.5**	1.4			**5.4**	1.4
svea	**1.3**	1.1	**2.1**	2.0	**1.7**	2.9
vnad	**4.4**	1.1			**5.2**	2.5

long time series, where uplift rate and uncertainty were derived using the CATS software (Williams 2008). Uplift rates at the majority of the GPS sites agree within uncertainty, except syog (Syowa), where the REGINA value is between that from the other two studies. The uncertainty limits for the REGINA value and the Argus et al. (2014) just meet at 0.9 mm/yr, even when allowing for the ~0.5 mm difference in reference frames, but the Thomas et al. (2011) value does not. This may be due to the fact that Thomas et al. (2011) estimate two offsets in the series. Table 3 shows uplift rate comparisons for sites where the 'prop,prop' method was used; the noise characteristics are derived from median values from CATS software results for longer site records and then propagated in the parameter estimation in which annual and semi-annual parameters were also estimated along with the trend. Again, the rates agree within uncertainty, except for site belg where there is a disagreement with Thomas et al. (2011). This may be due to their shorter data span. Table 4 shows comparisons for sites where the REGINA rates and uncertainties have been manually evaluated based on the spread of rates obtained by sub-sampling the time series ('rman' method). There is a large difference (over 10 mm/yr) in the values at capf (Cape Framnes) between the REGINA value (4.0 ± 1.4 mm/yr) and the Argus et al. (2014) value (15.0 ± 4.2 mm/yr). Interestingly, the Wolstencroft et al. (2015) rate values for bean, gmez, lntk, mkib, and trve are all systematically higher than the REGINA values, by an average of just over 3 mm/yr, and the uncertainties we assigned are also several times larger. [R1_370] The systematic differences between Wolstencroft et al. (2015) and the REGINA values for Palmer Land are currently unexplained and a matter of ongoing investigation. ~~For more detailed analysis of rates and time series at individual sites, see Petrie et al. (in prep b).~~

Table 4. Uplift rates y^u and associated uncertainties σ^u (mm/yr) for selected sites where uplift rates are manually evaluated based on the spread of rates obtained by sub-sampling the time series ('rman' method), compared to data published by Thomas et al. (2011), Argus et al. (2014), Wolstencroft et al. (2015). See also 'rman' sites in Table Appendix A.4, Table A.2.

Site	REGINA		Thomas et al. (2011)		Argus et al. (2014)		Wolstencroft et al. (2015)	
	y^u	σ^u	y^u	σ^u	y^u	σ^u	y^u	σ^u
bren	**3.1**	1.1	**3.9**	1.6	**2.1**	3.7	**3.2**	0.8
capf	**4.0**	1.4			**15.0**	4.2		
dav1	**-1.6**	0.6	**-0.9**	0.5	**–0.8**	1.0		
mait	**0.4**	1.1	**0.1**	0.6	**1.3**	0.7		
mbl3	**1.3**	17.9	**0.1**	2.0				
bean	**2.1**	4.3					**7.5**	1.2
gmez	**1.5**	4.8					**5.7**	0.8
lntk	**4.6**	3.1					**6.0**	0.7
mkib	**4.7**	2.6					**6.9**	0.5
trve	**2.5**	5.6					**4.7**	0.6

Data availability

The GPS data and related code are directly accessible in the Pangaea repository, http://hs.pangaea.de/model/Sasgen-etal_2017/In_situ_GPS_uplift_rates.zip

3.2 *Bedrock uplift rates*

Bedrock uplift rates derived for the REGINA project are available in the text file "REGINA_rates_full.txt", as presented in Table A.2 and A.3 of the Appendix A.4. The files "REGINA_rates_03-13.txt" and "REGINA_rates_03-09.txt" contain subsets of the data, with the temporal coverage limited to 2003-2013.5 and 2003-2009, respectively. The files are organized as follows:

3.2.1

Lon [°], Lat [°], uplift rate [mm/yr], uncertainty of the uplift rate [mm/yr], GPS site ID

These *.txt files are the input to the clustering script described below. No elastic correction has been applied.

3.2.2 *Clustering script*

In addition to the uplift rates for individual GPS sites, we provide a *bash* script "cluster.sh" for clustering the heterogeneous data according to their geographic locations, for a pre-defined threshold value. The idea is to reduce stochastic and geophysical noise of neighboring stations in order to obtain uplift rates that are better regional representations for the length scale recovered with GRACE (ca. 200 km). In an iterative procedure, the script selects neighboring sites within a threshold ranging from 10-220 km [R1_361] and calculates the weighted average of the uplift rates and a simple ~~uplift~~ average [R1_361] of the stations locations. Input to the script are the REGINA rate files, specified in the previous Section 3.2.1. Further details and the application to the GPS data set can be found in REGINA paper II (Sasgen et al., ~~submitted~~2017) [R1_361]. Note that the script relies on the open-source program suite Generic Mapping Tools, http://gmt.soest.hawaii.edu/ (Wessel et al. 2013). Similar clustering can be achieved with the function *kmeans* in Matlab® or its open-source alternative GNU Octave.

3.2.3 *GPS time series*

The GPS time series were created as part of the RATES project, not solely the REGINA study. ~~They will be made available along with the detailed descriptions in Petrie at al. (in prep b). The time series of vertical bedrock displacement will then be accessible here: [LINK].~~The data can be obtained upon request from co-author Dr. Elizabeth Petrie.

4. Gravimetry data analysis

We investigate the Release 5 (RL05) GRACE coefficients of the Centre for Space Research (CSR; Bettadpur, 2012) and the German Research Centre for Geosciences (GFZ; Dahle, 2013), provided up to spherical-harmonic degree and order j_{max}=96 and 90 respectively in the Science Data System (SDS). For reasons of comparison, we adopt j_{max}=90 for both GRACE solutions. A temporal linear trend in the ocean bottom pressure variations modeled by the atmospheric and oceanic background models (GAD) was re-added to the monthly solutions, according the GRACE Science and Data System recommendation (Dobslaw et al. 2013). The GRACE coefficients C_{20} were replaced by estimates from Satellite Laser Ranging (SLR) provided by Cheng et al. (2013). In our analysis we apply the cut-off degrees j_{max}=50, which has been commonly used, as well as $j_{max} = 90$, which is considered experimental in terms of the remaining signal content.

The determination of the rate of the gravity field change over Antarctica follows the scheme sketched in Fig. 3. The rate of the gravity field change, expressed as equivalent water height variations, is estimated in the spatial domain by adjusting a six-parameter function consisting of a constant, a temporal linear trend and annual and semi-annual harmonic amplitudes. A quadratic term was not co-estimated due to the project's focus on the rates (i.e. temporal linear trends). It should be stated that including a quadratic term would slightly reduce the residual uncertainties, particularly in the Amundsen Sea Sector, where an ice-dynamic [R1_476] acceleration of mass balance rates occurs that is not accounted for by ~~interannual~~ non-linear [R1_476] SMB variations of the ice sheet (see Section 4.2).

The post-processing of the GRACE coefficients follows three main steps:

Step 1: Optimization of de-striping filter

Due to effects like the propagation of measurement noise and temporal aliasing, a large proportion of the variations contained in the monthly solutions is related to noise. The noise of the monthly solutions is lowest close to the pole and exhibits a characteristic north-south

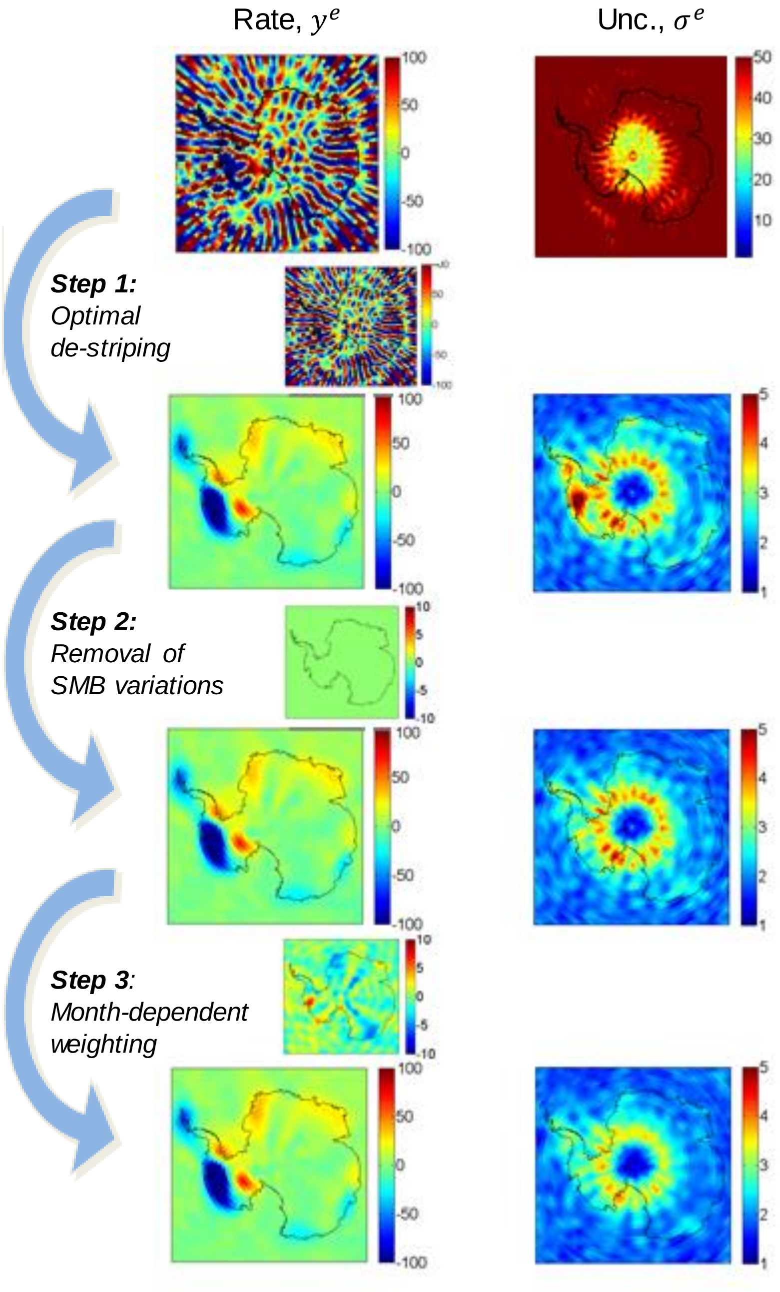

Figure 3. Post-processing steps applied to the GRACE gravity fields; shown is the impact on the gravity field rate y^g (left) and the associated RMS uncertainty σ^g (right). Small maps show change in the gravity field rate between two subsequent steps. Color scale is mm w.e./yr. GRACE data is GFZ RL05a.

oriented stripe pattern. This is visible in the gravity field rate and the propagated Root-Mean-Square (RMS) uncertainties shown in Fig. 3. In order to remove the stripe pattern, we apply the de-correlation filter of Swenson & Wahr (2006) (hereinafter, “Swenson filter”) specifically tuned to optimize the recovery of the gravity field rate over the region of Antarctica, which is detailed in Section 4.1. Fig. 3 shows that the de-striping procedure reduces the RMS uncertainty of the rate by approximately one order of magnitude.

Step 2: Reduction of ~~interannual~~ non-linear mass variations [R1_476]

For isolating gravity field rates, the second step in the processing is the reduction of de-trended variations of the surface mass balance, caused by accumulation events. The data set used for this purposes is the RACMO2/ANT (Lenaerts et al 2012) converted into monthly sets of spherical harmonic coefficients. The reduction of these ~~interannual~~ accumulation variations [R1_476] does not change the temporal linear trend, but it reduces RMS uncertainties especially in coastal regions (Fig. 3). Details are provided in Section 4.2.

Step 3: Month-dependent weighting

The performance of the GRACE satellite system was weaker in the early mission phase due to issues with the star cameras of the satellites (*C. Dahle, GFZ, pers. comm.*; Fig. 5). A rate estimate with uniform weighting of all months does not account for these variations. Therefore, in the last step, month-dependent uncertainties are estimated and applied as weights during the linear regression of the temporal linear trend. This slightly changes both the resulting rate estimate, as well as its RMS uncertainties. Details are provided in Section 4.3.

Finally, after post-processing and evaluation of the gravity field rate (Section 4.4), we select the GRACE release and cut-off degree providing the lowest uncertainty level (Section 4.5) as reference input for our joint inversion for present-day ice-mass change detailed in REGINA paper II (Sasgen et al. 2017).

4.1 *Optimization of de-striping filter*

The Swenson filter has been proven to effectively reduce the typical north-south correlated error structures of GRACE monthly solutions. The filter is based on the observation that these structures correspond to correlated patterns in the spherical harmonic domain, namely correlations within the coefficients of the same order and even degree, or respectively, odd degrees (Swenson & Wahr, 2006). The standard way of fitting and removing these patterns is by adjusting polynomials to the respective sequences of spherical harmonic coefficients, independently for individual months. Parameters to choose are the degree of the polynomial n_{pol} and the minimum order m_{start} starting from which this procedure is applied. In principle, a higher degree polynomial reduces the variability of coefficients of even / odd degree, and results, also at lower minimum order, in stronger filtering – however, the behavior of the filter may differ for regional applications, as discussed below. Note that tuning of other parameters has been presented, e.g. the window width (Duan et al. 2009) or the degree range to which the filter is applied. Chambers and Bonin (2012) have assessed these parameter options with regard to the new GRACE RL05 solutions and global oceanic signals. Here, we perform a detailed analysis of the choice of the Swenson filter parameters in order to optimize the signal-to-noise characteristics of the rate of the gravity-field change over Antarctica. ~~The resulting gravity field rates are later used in the joint inversion for present-day ice-mass change and GIA described in REGINA Part II.~~

We assess signal corruption by applying the filter to a synthetic test signal, which is based on high-resolution elevation rates from satellite altimetry and reflects the prevailing signatures of present-day ice-change with sufficient realism. For each choice of filter parameters, the signal corruption is assessed as the RMS difference between the original and the filtered

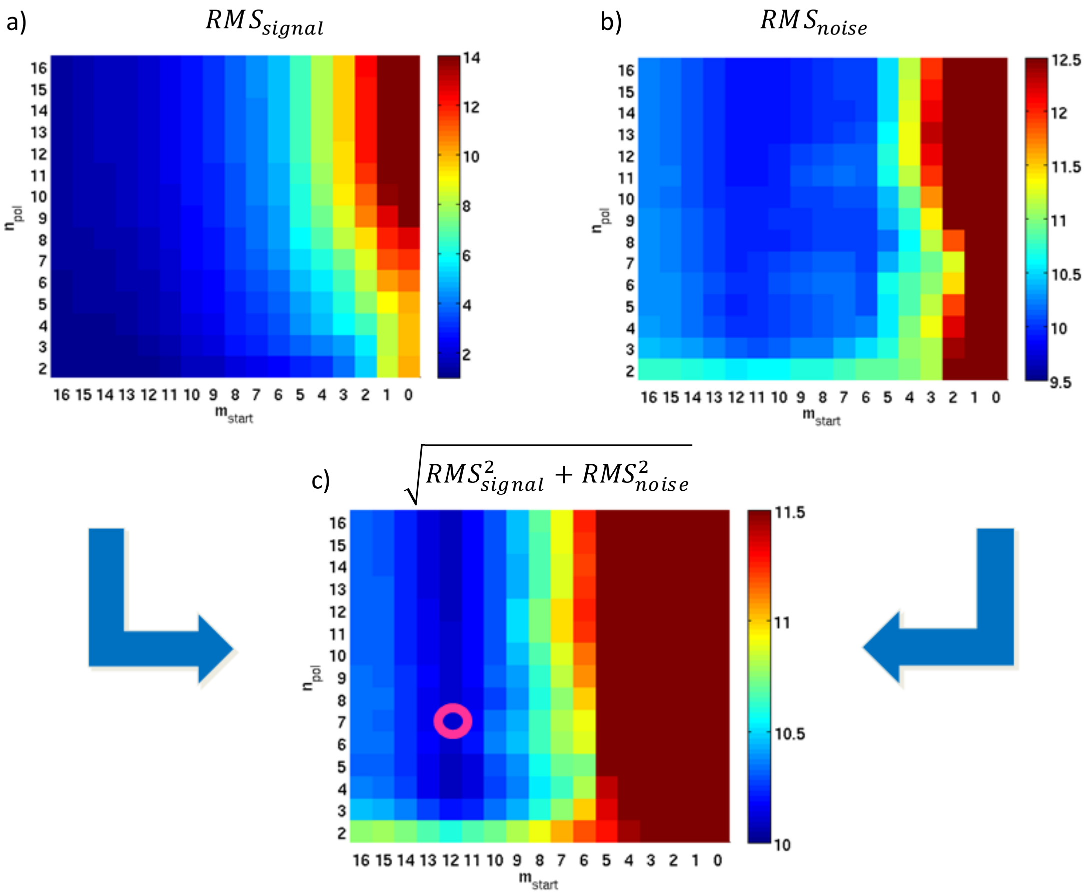

Figure 4. Effect of Swenson filter parameters m_{start} and n_{pol} on a) signal corruption, b) noise reduction and c) combined effect on signal and noise. RMS residuals are shown for the gravity field rates in (mm w.e./yr). The optimal choice of filter parameters m_{start} = 12 and n_{pol} = 7 is indicated as circle. Results are shown for GFZ RL05a with j_{max} = 90.

synthetic signal, RMS_{signal}. The RMS is evaluated in terms of water-equivalent height per year for the signal components within the region south of 60°S latitude.

For assessing the noise and noise reduction in the filtered fields, we face the task of separating the noise from the geophysical signals in the gravity field rates derived from GRACE. Here we attempt such a separation by reducing *a priori* information on the rate of ice mass change from the GRACE fields and considering the residual as an upper bound representation of noise. The *a priori* information is, again, based on elevation rates. For the noise assessment we then take the RMS of the residual rates in terms of water equivalent height per year, RMS_{noise}, again for the region south of 60°S latitude. Since the residual gravity field rates may still contain some geophysical signal, we consider this noise estimate as an upper bound for the true GRACE uncertainties. It should be stated that, after the Swenson filtering, an additional Gaussian filtering is applied to the signal and noise models with a 200 km filter width, which was determined to be the optimal smoothing half-width for the signal-to-noise ratio in the GRACE spectra by Wiener optimal filtering (Sasgen et al. 2006) as reflected in the degree-amplitude spectrum.

Fig. 4 shows the assessed signal corruption and noise reduction as a function of the two Swenson filter parameter choices, the polynomial degree n_{pol} and the minimum order m_{start}. The results are shown for the gravity field expanded to degree and order $j_{max} = 90$ of the GFZ RL05a coefficients, even though using $j_{max} = 50$ and CSR RL05 yields similar results. As expected, the signal corruption, RMS_{signal} increases with increasing strength of the Swenson filter, that is with increasing n_{pol} and the decreasing minimum order m_{start}. In terms of noise reduction, we see as expected that stronger filtering (increasing n_{pol}; decreasing m_{start}) decreases the RMS_{noise} (Fig. 4). [R1_470]~~,~~ ~~H~~However, we find that ~~only for the~~ for ~~range of filter parameters with $m_{start} \geq 10$. For~~ filter parameters $m_{start} < 10$ this pattern is reversed, and RMS_{noise}. A closer analysis indicates that the consideration of the low orders into the Swenson filtering transfers energy (both from signal and noise) from low-to-mid latitudes to the Polar Regions, which ~~. This~~ leads to a considerable signal corruption over the region of interest. ~~that is only avoided~~ We avoid this degradation by limiting the range of filter parameters in ~~this~~ the subsequent ~~regional analysis~~optimization of the gravity trends to $m_{start} \geq 10$.

To define the optimal filter parameters a quadratic sum of the signal corruption and noise reduction is computed, allowing us to balance both effects, the optimal values are $m_{start} = 12$ and $n_{pol} = 7$ as indicated in Fig. 4c. These filter parameters are subsequently used. For comparison it is stated that Chambers & Bonin, 2012 ~~find~~ found $m_{start} = 15$ and $n_{pol} = 4$ ~~as~~ to be optimal for oceanic applications. [R1_511] Note that the signal corruption is assessed only to optimize the de-striping filter. Possible signal degradation due to de-striping is not included in the uncertainty estimate of the optimally filtered GRACE trends. However, signal loss due to the additional smoothing with a 200 km Gaussian filter is accounted for by applying the same filter to the viscoelastic response functions, as well as the altimetry-based input fields (Appendix A.5).

4.2 *Reduction of ~~interannual~~ non-linear mass variations*

~~Interannual variations are a major constituent of t~~The temporal variations of the Antarctic gravity field show a strong year-to-year fluctuation, apart from the linear trend (Wouters et al. 2014) [R1_476]. A large portion of the non-linear signal in geodetic mass and volume time series is well explained by modelled SMB fluctuations (Sasgen et al. 2010; Horwath et al. 2012). Towards the ultimate goal of isolating the linear GIA signal from time series of mass change, we removed non-linear effects of modelled SMB variations from the GRACE time series; for this we calculate the *monthly cumulative SMB anomalies* with respect to the time period 1979 to 2012 obtained from RACMO2/ANT (Lenaerts et al. 2012).

We then transfer the monthly cumulative SMB anomalies in terms of their water-equivalent height change into the spherical harmonic domain and subtract them from the monthly GRACE coefficients. In principle, the reduction of the SMB variations from the GRACE time interval has two effects: first, it may change the overall gravity field rate derived from GRACE, depending on the assumption of the SMB reference period. Ideally, the reference period reflects a state of the ice sheet in which input by SMB equals the outflow by ice discharge, and SMB anomalies estimated for today reflect the SMB component of the mass imbalance. However, any bias in the SMB in the reference period leads to an artificial trend in the ice sheet mass balance attributed to SMB. This is an undesired effect, and to avoid it we de-trend the cumulative SMB time series for the time interval coeval to the GRACE analysis (February 2003 to October 2009), before subtracting it from the GRACE gravity fields, ~~rates derived from~~ yielding zero difference in the gravity field rates ~~GRACE (zero difference for~~ before and after processing *Step 2*~~,~~ (Fig. 3) [R1_402]. The second effect is the reduction of the post-fit RMS residual for this known temporal signal variation. After reducing the SMB variations, the propagated RMS uncertainty of the derived gravity field rate becomes closer to the uncertainty level of the GRACE monthly solutions (Fig. 3).

4.3 Month-dependent weighting

The quality of GRACE monthly solutions changes with time, for example due to changing orbital sampling patterns (Swenson & Wahr 2006). Fig. 5 shows the temporal evolution of RMS

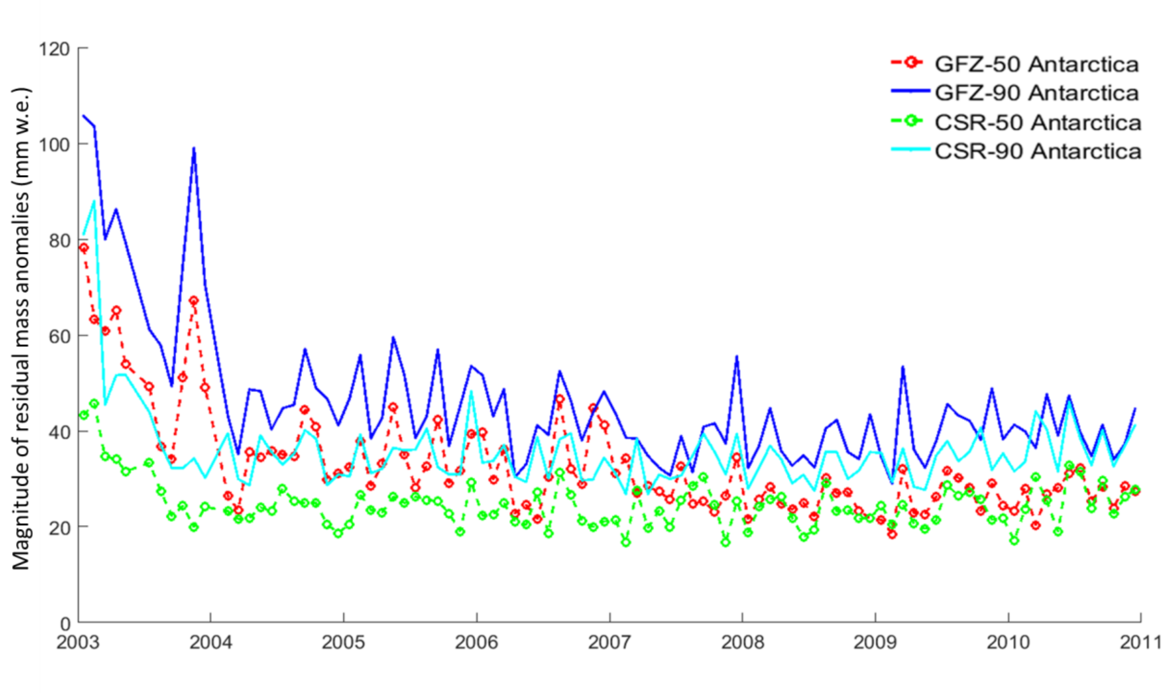

Figure 5 [R1_495]. ~~RMS~~ Residual mass anomaly ~~uncertainty~~ of monthly GRACE gravity fields~~-~~for 2003-2011, averaged over the Antarctic region south of $-60°S$ *latitude. Shown are results for GFZ RL05a and CSR RL05 and* $j_{max} = 50$ *and* $j_{max} = 90$.

uncertainties of the monthly GRACE gravity fields in the Antarctic region; ~~.~~ s~~S~~hown are residual mass anomalies, integrated over Antarctica, after the grid-based removal of the temporal linear trend and annual oscillation components and applying the filtering described in *Step 1* and removing the SMB fluctuations in Step 2 [R1_495]. Note than an annual oscillation component is included to remove possible seasonal fluctuations in SMB not captured by the regional climate model [R1_495]. However, omitting the annual oscillation component yields similar results.-The residual monthly mass anomalies are attributed to noise and are used To improve the accuracy of the estimate of the gravity field rate, we include monthly uncertainties as weights in our least-squares linear regression, applied as Step 3 of the GRACE processing. Fig. 5 shows that these uncertainties are higher during early 2003. Applying the monthly dependent weighting has the effect of reducing the influence of the first months of the year 2003 on the estimated gravity field rate, which is similar to shortening the time series, given the relatively large uncertainties. AlsoAs expected, the post-fit RMS uncertainty associated with the rate reduces, if the early months of the year 2003 are excluded [R1_509]. , indicating that down-weighting the months from early 2003 is more beneficial than retaining a longer time series. Altogether, the month-dependent weighting reduces the magnitude of stripe patterns characteristic for the uncertainty of GRACE monthly solutions, and yields a more accurate realistic representation estimate of the of propagated RMS uncertainty associated with the gravity field rates (Fig. 3) [R1_514].

4.4 *Gravity field rate and uncertainty assessment*

Fig. 6 shows the estimated RMS uncertainty of the gravity field rate over Antarctica, after post-processing. It is evident that the largest uncertainties are located in a ring south of $-80°$S latitude. This is explained by the design of the Swenson filter; little or no noise reduction is achieved close to the poles, as the gravity field is represented by near-zonal coefficients, which

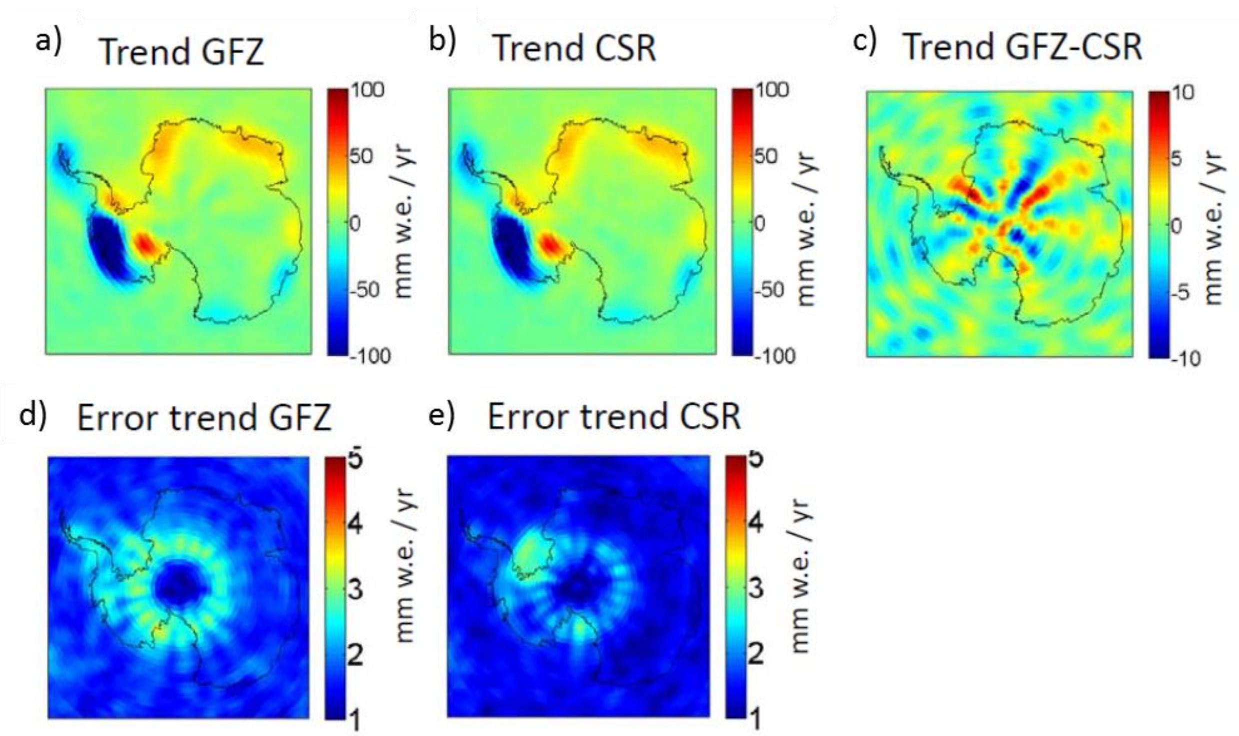

Figure 6. Linear trend in the GRACE gravity fields for the years 2003-2009; a) GFZ RL05a, b) CSR RL05, c) difference between rates from GFZ RL05 and CSR RL05, propagated d) RMS uncertainty for GFZ RL05a and e) RMS uncertainty for CSR RL05.

pass the filter mostly unchanged ($m_{start} = 12$). ~~It is observed that e~~Extending the kernel of the Swenson filter to these near-zonal coefficients ($m_{start} \leq 10$) creates high signal corruption and is not suitable for the optimal rate estimate over Antarctica (see Section 4.1). Larger uncertainties are also estimated for the Ronne and Ross ice shelf areas, which are most likely a consequence of incomplete removal of the ocean tide signal during the GRACE de-aliasing procedure (Dobslaw et al. 2013). It should also be stated that the RMS uncertainty estimate does not include possible systematic errors in the GRACE solutions, e.g. due to a long-term drift behavior of the observing system.

Selection of GRACE release

Our evaluation of the monthly GRACE uncertainties (Fig. 5), as well as the propagated RMS uncertainty of the temporal linear trend (Fig. 6) indicates that the lowest noise level for the Antarctic gravity field rate (February 2003 to October 2009) is currently achieved with GRACE coefficients of CSR RL05, expanded to $j_{max} = 50$. We therefore refrain from including coefficients with $j_{max} > 50$ in order not to ~~comprise~~ compromise the rate estimates by unnecessarily increasing the noise level (see Appendix A.5, Fig. A.3). We adopt CSR RL05 with $j_{max} = 50$ as our preferred solutions for the representation of the gravity field rates over Antarctica, even though GFZ RL05 with $j_{max} = 50$ yields very similar rates (Fig. 6). This choice is supported by the joint inversion, as CSR RL05 with $j_{max} = 50$ provides the highest level of consistency (lowest residual misfit) with the altimetry and GPS data sets (see REGINA Part II, Sasgen et al. 2017, Supplementary Information, Section S.3), which we interpret to indicate ~~as~~ a minimum of spurious signals in the trends. To account for the uncertainty related to our choice of the solution, we consider not only RMS uncertainties of the GRACE rates but also solution differences, in the uncertainty of the final GIA estimate (Fig. 6). The solution difference represent the absolute deviation between trends from GFZ RL05 and CSR RL05 (February 2003 to October 2009, cut-off degree $j_{max} = 50$). These are then summed up squared with the propagated RMS uncertainties. It is acknowledged that the solution differences contain systematic noise arising from the GRACE processing; the pattern and magnitude may change over time. However, they provide a measure how much the results will change, if a GRACE release alternative to CSR RL05 is considered. The difference between GRACE rates filtered with Gaussian smoothing of 200 km and the optimized Swenson filter together with Gaussian smoothing of 200 km is shown in the Appendix A.5, Fig. A.4.

4.6 *Data availability*

The gravity data and related code are directly accessible in the Pangaea repository, http://hs.pangaea.de/model/Sasgen-etal_2017/Geoid-height_change_from_GRACE_satellite.zip

4.6.1 *Stokes coefficients of gravity field change*

The monthly GRACE gravity field solutions from the Data System Centers GFZ and CSR are available under ftp://podaac.jpl.nasa.gov/allData/grace/L2/ or http://isdc.gfz-potsdam.de/ as spherical harmonic (SH) expansion coefficients of the gravitations potential (Stokes confidents). More information is available in Bettadpur (2012). The data archive contains temporal linear trends of the fully normalized Stokes coefficients in the 'geodetic norm' (Heiskanen & Moritz, 1967), complete to degree and order 90, inferred from these time series according to Section 4~~,~~. We provide data for GFZ RL05 and CSR RL05, for the time period 2003-2009 and 2003-2013, and for various combinations of filtering. The coefficients are organized as:

[Degree j], [Order m], [c_jm], [s_jm]

4.6.2 *Code for de-striping filtering*

The Matlab® function "KFF_filt" performs decorrelation filtering for sets of spherical harmonic coefficients, typically from GRACE gravity field solutions, after the idea of Swenson & Wahr (2006). An open-source alternative to Matlab® is GNU Octave https://www.gnu.org/software/octave/. The function is called as KFF_filt = swenson_filter_2(KFF, ord_min, deg_poly, factorvec, maxdeg), where variables ord_min and deg_poly equal m_{start} and n_{pol}, respectively, in Section 4. KFF contains the sets of spherical harmonic coefficients in the 'triangular' format (not memory-efficient but intuitive). For example, for a set of coefficients with maximum degree $j_{max} = 3$ and maximum order $m_{max} = 3$, the set of coefficients is stored in a $j_{max} \times m_{max}$ matrix in the following way:

```
% KFF = [0    0    0    c_00  0     0     0;
%        0    0    s_11 c_10  c_11  0     0;
%        0    s_22 s_21 c_20  c_21  c_22  0;
%        s_33 s_32 s_31 c_30  c_31  c_32  c_33]
```

5. Viscoelastic modelling

The Earth structure of Antarctica is characterized by a strong dichotomy between east and west, separated along the Transantarctic Mountains (e.g. Morelli & Danesi, 2004). Recent seismic studies have produced refined maps of crustal thicknesses also showing slower upper-mantle seismic velocities in West Antarctica, indicating a thin elastic lithosphere and reduced mantle viscosity (An et al. 2015; Heeszel et al. 2016). Moreover, yield strength envelopes of the Earth's crust and mantle suggest the possibility of a viscously deforming layer (DL) in the lower part of the crustal lithosphere (Ranalli & Murphy, 1987), a few tens of km thick and with viscosities as low as 10^{17} Pa s (Schotman et al., 2008). High geothermal heat flux is in agreement with the seismic inferences of a thin elastic lithosphere and low mantle viscosity, and would favor the presence of such a DL also in West Antarctica (Shapiro & Ritzwoller 2004; Schroeder et al. 2014).

The choice of the viscoelastic modelling approach used to determine load-induced surface displacements and gravitational perturbations is governed by three main requirements; i) to accommodate ~~a~~ lateral variations in Earth viscosity, ii) to allow for Earth structures with thin elastic lithosphere and low viscosity layers, in particular including a DL, and iii) to provide viscoelastic response functions for the joint inversion of the satellite data described in REGINA paper II (Sasgen et al. 2017~~*submitted*~~). With regard to point iii) it should be mentioned that the viscoelastic response functions provide a geophysical meaningful way to relate surface displacement and gravity field changes, considering also dynamic density changes within the Earth's interior . Moreover, it allows us to consider the changes in the ratio of surface-displacement and gravity field changes caused by the Earth structure, in particular, the lithosphere thickness. Another advantage is that different filtering can be applied to the viscoelastic response functions in order to match the filtering of the input data set, avoiding the introduction related biases (Appendix A.5)[R1_653].

To meet these requirements, we adopt the time-domain approach (Martinec 2000) for calculating viscoelastic response functions of a Maxell continuum to the forcing exerted by normalized disc-loads of constant radius. Then, the magnitudes and spatial distribution of the surface loads are adjusted according to the satellite data to obtain the full GIA signal for Antarctica. The forward modelling of viscoelastic response functions is a classic topic in sold Earth modelling (e.g. Peltier & Andrews, 1976), however, their application to inverting multiple-satellite observations for present and past ice sheet mass changes is new and applicable to other regions, such as Greenland or Alaska.

The viscoelastic response function approach allows for high spatial resolution at low computational cost in the numerical discretization of the Earth structure as well as in the representation of the load and the response. In addition, we can accommodate a high temporal resolution, which is required when considering low viscosities and associated relaxation times of only a few decades. The spherical harmonic cut-off degree for the simulations shown in the following is $j_{max} = 2048$ (ca. 10 km).

5.1 *Load model parameters*

The load function $\sigma(t, \vartheta)$ is disc shaped with a constant radius of ca. 63 km. The radius of 63 km matches the mean radius of the discs south of 60°S of the geodesic grid (here, ICON 1.2 grid, status 2007, e.g. Wan et al., 2013), which underlie the joint inversion of the altimetry, gravimetry and GPS observations (see REGINA paper II, Sasgen et al. ~~submitted~~2017.). The resolution of the geodesic grid is chosen to allow for an adequate representation of the load and viscoelastic response with regard to the input data sets, while minimizing the computational cost. The disc load experiment consists of a linear increase in the ice thickness at a rate of 0.5 m/yr continuing until a new dynamic equilibrium state between load and response is reached. [R2_658] After the application of the constant loading rate, two extra time steps are done with no loading change to give the purely viscoelastic response. For West Antarctica, the loading rate is held constant for 2000 years, for East Antarctica it is 15,000 years, which are longer times than needed to reach dynamic equilibrium (see Appendix A.8). With reference to the assumed ice density of 910 kg/m³, this thickness increase corresponds to a mass gain of *ca.* 5.6 Gt/yr. Then, to obtain the signal component of the viscous Earth response only, the elastic response and the direct gravitational attraction of the load are subtracted.

The experiment is designed as an *increasing* load, for example representative for the ceasing motion of the Kamb Ice Stream (Ice Stream C; Retzlaff & Bentley, 1993), West Antarctica. Due to linearity of the viscoelastic field equations, it is not necessary to calculate separately the equivalent *unloading* experiment, $-\sigma(t,\vartheta)$, for example corresponding to the past and present glacier retreat of the Amundsen Sea Sector, West Antarctica (Bentley et al. 2014 and Rignot et al. 2014, respectively). Among others, the combined inversion of the altimetry, gravity and GPS data (REGINA paper II, Sasgen et al. 2017) solves for the magnitude and the sign of the load, allowing for ice advance as well as ice retreat.

5.2 *Earth model parameters*

We set up an ensemble of 58 simulations representing different parameterizations of the viscosity structure (Table 5), split into West Antarctica (56 simulations) and East Antarctica (2 simulations). The ensemble approximately covers the range of values of the viscosity and lithosphere thickness inferred from Priestley & McKenzie (2013) [R1_696]. For West Antarctica, varied parameters are the lithosphere thickness, h_L (30 to 90 km in steps of 10 km), the asthenosphere viscosity (1×10^{18} Pa s to 3×10^{19} Pa s in four steps), and the presence of a ductile lower crust, DL, with 10^{18} Pa s. For East Antarctica, we employ parameter combinations appropriate for its cratonic origin with h_L of 150 km and 200 km, and an asthenosphere viscosity equivalent to the upper-mantle viscosity of 5×10^{20} Pa s. These values lie in the range of previously applied viscosity values in Antarctica (Nield et al. 2012; Whitehouse et al., 2012; Ivins et al., 2013; van der Wal et al., 2015). For the radial layering of the elastic properties, we adopt the Preliminary Reference Earth Model (PREM; Dziewonski & Anderson 1981).

Table 5. Earth model parameters associated with the disc load ensemble simulations. The viscoelastic parameterization of the Earth model is discretized in six radial layers; upper and lower crust, mantle lithosphere, asthenosphere, upper and lower mantle. The lower mantle extends down to the core mantle boundary (CMB; at the depth of 2763 km). Elastic layers are represented by a quasi-infinite viscosity of 10^{30} Pa s.

Layer	Depth (km)	Viscosity (Pa s)	Unique param. val.
West Antarctica			
Upper crust	20	10^{30}	1
Lower crust DL [yes/no]	30	[10^{30}/10^{18}]	2
Mantle lithosphere	[30, 90, steps of 10]	10^{30}	7
Asthenosphere	200	[1×10^{18}, 3×10^{18}, 1×10^{19}, 3×10^{19}]	4
Upper mantle	670	5×10^{20}	1
Lower mantle	CMB	2×10^{22}	1
Number of simulations West Antarctica			56
East Antarctica			
Crust	30	10^{30}	1
Mantle lithosphere	[150, 200]	10^{30}	2
Upper mantle	670	5×10^{20}	1
Lower mantle to CMB	CMB	2×10^{22}	1
Number of simulations East Antarctica			**2**
Elastic earth			
Crust and mantle to CMB	CMB	10^{30}	**1**
Total number of simulations			**59**

Later, in the joint inversion, the distribution of viscoelastic response functions is based on the Earth structure model of Priestley & McKenzie (2013). Priestley & McKenzie (2013) provide a global distribution of viscosity values up to a depth of 400 km, which is sampled at the location of the geodesic grid. We then define a threshold value for the viscosity (here, 10^{22} Pas) above which the Earth response is considered purely elastic and infer the associated thickness of the elastic lithosphere. The impact on the final joint inversion estimate of changing the threshold value of 10 [22] Pas is presented in REGINA Paper II (Fig. S4 in Sasgen et al. 2017) [R1_712].~~.~~Note that the Earth response in the equilibrium state only depends on the lithosphere thickness (independent of viscosity), which is therefore considered as the main Earth model parameter~~s~~ in the joint inversion. Further details are presented in REGINA paper II, Sasgen et al. (2017).

5.3 *Gravity and displacement rate response functions*

The calculated response functions for surface deformation (radial displacement) and gravity (geoid height change) are discretized along 1507 latitudinal points within the range $0 \leq \vartheta \leq 90$. Simulations are typically run over 2 kyr with a temporal resolution of $\Delta t = 10$ yr (plus two time steps with constant load thickness). For East Antarctic parameterizations, the simulation period was extended to 20 kyr due to the higher upper-mantle viscosities and associated slower relaxation. However, note that the ratio of geoid-height change versus radial displacement falls off to a factor of $1/e^2$ relative to the initial value [R1_700][R2_700] ~~-~~after ca. 2 kyr of simulation (Appendix A.6, Fig. A.5). The forcing expected in central East Antarctica is an increase in accumulation towards present-day conditions after ca. 7 ka BP (van Ommen et al. 2004), justifying also the use of equilibrium kernels for East Antarctica. The time derivatives of the radial displacement y^u ~~$\dot{u}$~~ and of the geoid height change y^g ~~$\dot{e}$~~ are calculated with a central difference scheme.

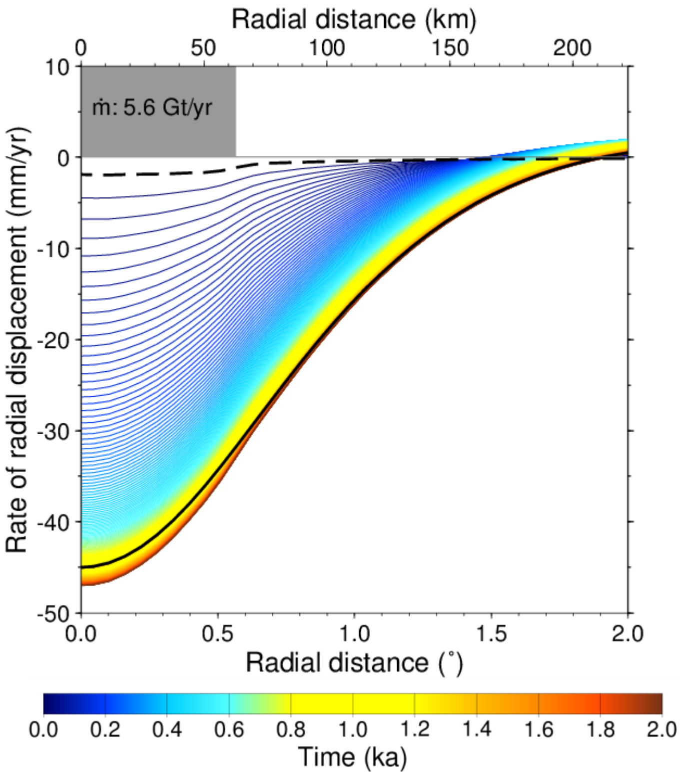

Figure 7. Displacement rates over the simulation period of 2 kyrs, for an exemplary set of Earth model parameters ($h_L = 30\ km$; $\eta_{AS} = 1 \times 10^{18}\ Pa\ s$). Shown is the load dimension (grey shading), as well as the instantaneous elastic response (dashed black line) and purely viscoelastic ~~relaxation~~ response ~~only~~ after 2 kyr ~~and~~ without ~~no~~ a load change (solid black line). The other curves show the rates for the time epoch indicated by the color scale.

Examples of response functions to the loading detailed in Section 5.1 for the rate of radial displacement, $y^{\dot{u}}$~~$\dot{u}$~~, and rate of geoid-height change,–y^{g}~~$\dot{e}$~~, are shown in Figs 7 and 8, respectively. Instantaneously, the increasing load, $\dot{\sigma}(t) = \text{const.}$, induces an elastic response that is characterized by subsidence and an increase in the direct gravitational potential (dashed lines in Fig. 7 and Fig. 8, respectively). This is the elastic response function adopted in the joint inversion. Note that the elastic response function will not differ between East and West Antarctica, as it is entirely based on the distribution of densities and elastic parameters provided by the PREM. As the load build-up continues, the instantaneous response is followed by the

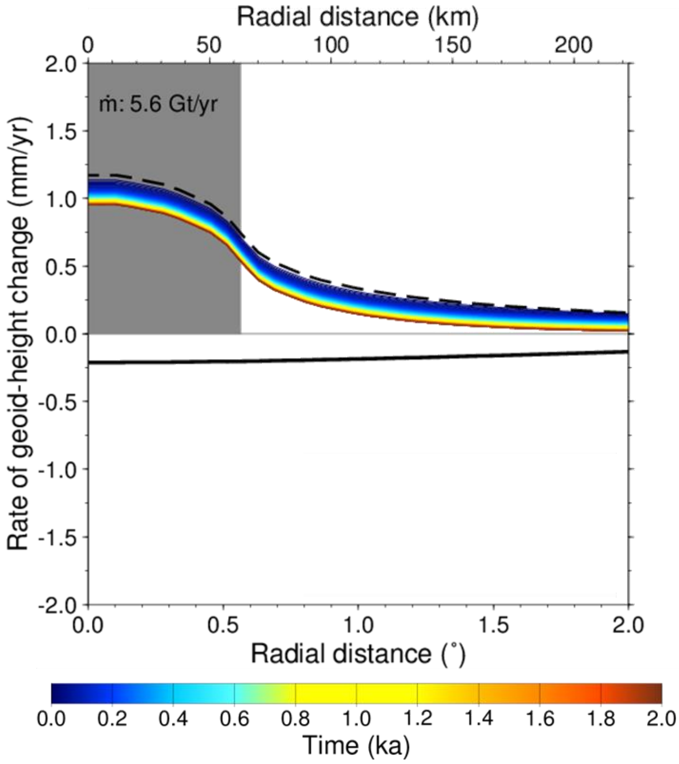

Figure 8. Same as Fig. 7, but for the rate of geoid-height change and Earth model parameters $h_L = 90\ km\ ;\ \eta_{AS} = 1 \times 10^{18}\ Pa\ s$. Note the change in sign in the rate when the increase in direct gravitational attraction through load increase ceases after 2 kyr (black solid line vs. colored lines).

viscoelastic response, which depends in timing and magnitude on the underlying lithosphere and viscosity structure, further increasing the displacement rates, y^u ~~$\dot{u}$~~ (blue to red lines in Fig. 7). The compensation by solid Earth deformation is reflected in the decreasing geoid rate, y^g ~~$\dot{e}$~~ (Fig. 8). After a certain time, which depends on the value of the asthenosphere viscosity, a new dynamic equilibrium state is reached at which $\dot{u}$ and $\dot{e}$ do not change in time any more. In the last two time steps, the load is kept constant ($\dot{\sigma}(t) = 0$), and the responses in $\dot{u}$ and $\dot{e}$ are only caused by the relaxation of the Earth's viscoelastic deformation (solid black line in Figs. 7 and 8), which is the viscoelastic response function adopted in the joint inversion.

5.4 *Discussion of effects of selected earth model parameterizations on GIA response*

Fig. 9 shows the response of $\dot{u}$ for four end-member sets of Earth model parameters with thick lithosphere, weak asthenosphere ($TkWk$: $h_L = 90\ km$; $\eta_{AS} = 1 \times 10^{18} Pa\ s$), thick lithosphere, strong asthenosphere ($TkSg$: $h_L = 90\ km$; $\eta_{AS} = 3 \times 10^{19} Pa\ s$), thin lithosphere, weak asthenosphere ($TnWk$: $h_L = 30\ km$; $\eta_{AS} = 1 \times 10^{18} Pa\ s$) and thick lithosphere, strong asthenosphere ($TnSg$: $h_L = 30\ km$; $\eta_{AS} = 3 \times 10^{19} Pa\ s$), without a ductile layer, DL. In this context, thick / thin and strong / weak refer to values in comparison to the 'average' value of the ensemble for West Antarctica; an elastic lithosphere of thickness 90 km (here, '*Tk*') is in the range of global average continental lithosphere usually applied in GIA studies (e.g. Peltier, 2004), or that of East Antarctica (150 to 200 km). Fig. 10 shows the response in $\dot{u}$ for the same end-member set of Earth model parameters with a DL included. It should be stated that the Earth structure with $h_L = 30$ km *and* a DL is considered very extreme, because in this case the ductile layer extends down to the asthenosphere and an elastic mantle lithosphere is missing.

Fig. 9 and 10 show that for the weak asthenosphere ($\eta_{AS} = 1 \times 10^{18}$ Pa s), viscoelastic deformation is visible already after one decade of loading (or unloading), leading to considerably larger subsidence rates compared to the purely elastic case even on very short time scales. For these Earth model parameters, a new dynamic equilibrium state is achieved within a few centuries. The rates of subsidence in this equilibrium then primarily depend on the support provided by the flexure of the elastic lithosphere.

For the extreme *TnWk* case, equilibrium rates of -45 mm/yr are achieved at the load centre, and considerable subsidence of -20 mm/yr already occurs after ten years of loading (Fig. 9). Increase in asthenosphere viscosity (*TnSg* case) reduces the viscous material transport and leads to a slower adjustment towards the dynamic equilibrium state, which takes more than 1 kyr. It should be stated that in our definition of the ensemble parameters, reducing the

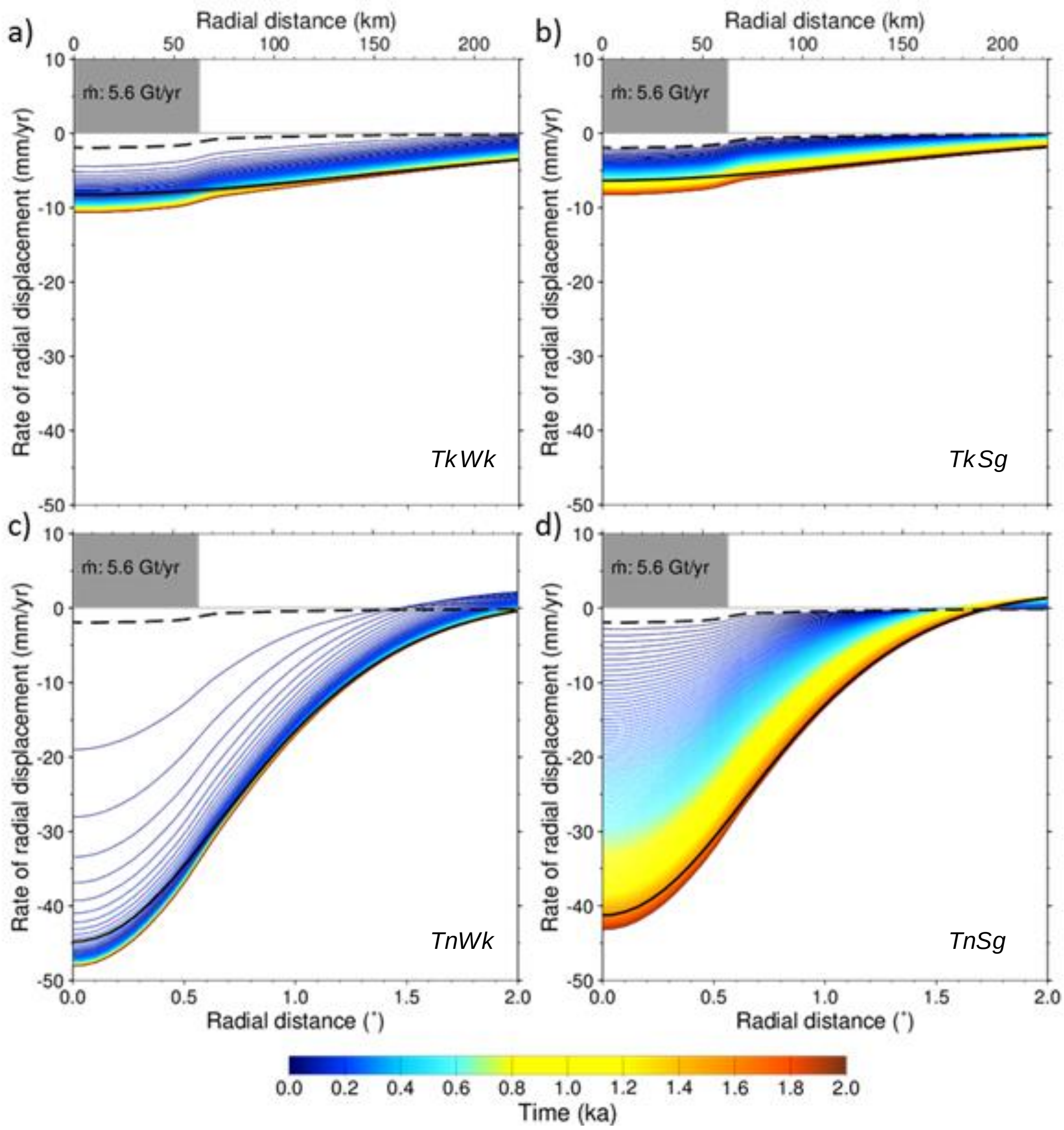

Figure 9. Same as Figure 7, but for four end-member sets of Earth model parameters, without a DL and lithosphere thickness / asthenosphere viscosity of a) $h_L = 90\ km$ / $\eta_{AS} = 1 \times 10^{18} Pa\ s$ (TkWk, b) $h_L = 90\ km$ / $\eta_{AS} = 3 \times 10^{19} Pa\ s$ (TkSg), c) $h_L = 30\ km$ / $\eta_{AS} = 1 \times 10^{18} Pa\ s$ (TnWk) and d) $h_L = 30\ km$ / $\eta_{AS} = 3 \times 10^{19} Pa\ s$ (TnWk).

lithosphere thickness in turn increases the thickness of the asthenosphere (bottom depth of asthenosphere is fixed), which facilitates lateral material transport inside the asthenosphere.

The consideration of the DL in the Earth structure causes a thinning of the effective elastic

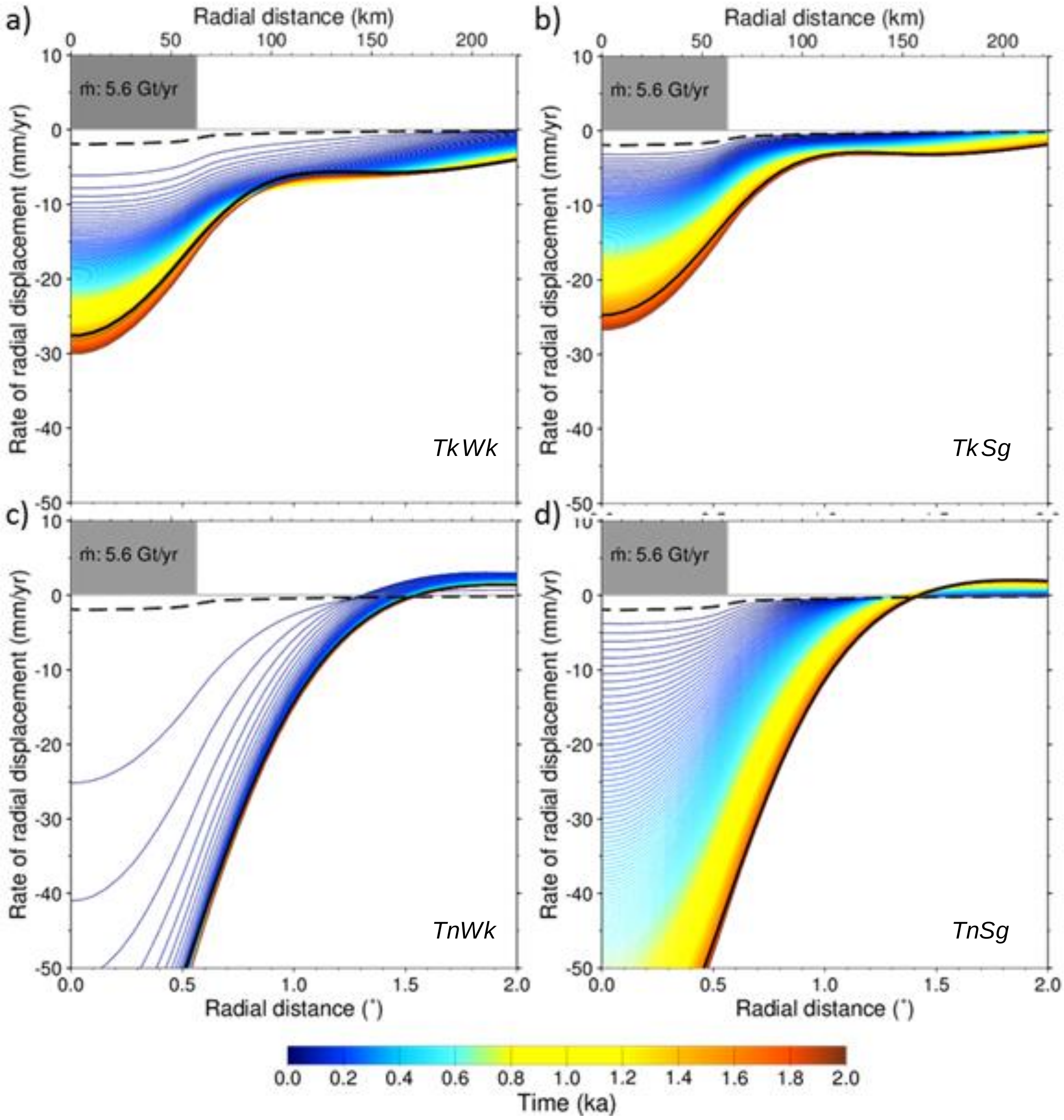

Figure 10. Same as Figure 9, a) TkWk, b) TkSg (b), TnWk (c) and TnSg (d), but with the Earth structure including a DL.

lithosphere. As a consequence, greater and more localized subsidence rates are produced for all sets of parameters (Fig. 10). Interestingly, in case of a thick elastic lithosphere (90 km), the radial displacement exhibits a local minimum at around 120 and 160 km distance from the load centre (Fig. 10), which is a consequence of the viscous material transport inside the ductile layer. The maximum equilibrium rate of −76 mm/yr is achieved for the *ThWk* case with DL, where the viscous deformation leads to rates of −25 mm/yr already after 10 yrs of loading.

5.5 *Assumptions and limitations*

Although the approach of modelling response functions to axisymmetric disc loads and subsequently superposing them is very efficient in terms of the computational cost, this simplification introduces some limitations. First, the superposition of response functions representing different Earth structures neglects the transmission of stresses between these regions — a problem that can only be resolved with fully three-dimensional solid Earth modelling (e.g. van der Wal et al., 2015). The largest impact for the displacement rates is expected in regions with lateral contrasts in lithosphere thickness and mantle viscosity such as the Transantarctic Mountains. Second, the constant disc radius of about 63 km implies that finer-scale deformation cannot be resolved. Although this resolution is adequate for interpreting GRACE data (spatial half-wavelength of *ca.* 200 km) smaller-scale loading excitement may be necessary for interpreting local GPS measurements near to the loading, particularly for the elastic response to present-day glacial changes. Furthermore, the viscoelastic response functions describe the Earth response in an equilibrium state for a constant rate of load change; if the load exhibits more complex temporal variations, this assumption is violated. Finally, it is assumed that the lithosphere thickness, upper- and lower-mantle viscosities are approximately known. [R1_795].

5.6 *Data availability*

The viscoelastic response functions and related ancillary data are directly accessible in the Pangaea repository:

http://hs.pangaea.de/model/Sasgen-etal_2017/Viscoelastic_response_functions.zip

5.6.1 *Viscoelastic kernels*

Output files contain 1507 latitudinal points (0≤ϑ ≤90) covering a region greater than the size of the Antarctic domain, as well 203 time steps of West Antarctica (213 time steps for East Antarctica, because of extending the simulation period to 15 kyrs). The time derivative of the radial displacement, u, is calculated with a central difference scheme, y^u ≔ [u(t+Δt/2)-u(t-Δt/2)]/Δt. The difference between two time steps is Δt=10 yr. The same applies to the rate of geoid-height change, y^g. Note that the load is constant during the last two time steps (no rate of change); therefore, the kernels represent the viscoelastic relaxations only, without the instantaneous elastic deformation or the direct gravitational attraction of the load.

The results are stored independently for the rheology of East and West Antarctica, the latter with and without a ductile layer in the elastic part of the lithosphere. The data are stored in a Matlab® file format, which is also readable with GNU Octave https://www.gnu.org/software/octave/ .

- 'Viscoel_response_WA_with_DL.mat' – Response functions for West Antarctica *with* ductile layer
- 'Viscoel_response_WA_no_DL.mat' – Response functions for West Antarctica *without* ductile layer
- 'Viscoel_response_EA_no_DL.mat' – Response functions for East Antarctica *without* ductile layer

- ‘Time_EA_rheo.mat / Time_WA_rheo.mat’ – Time [kyr] file related to response file for East and West Antarctica
- ‘Coord_Co-Latitude.mat’ – Co-latitude [°] of the response functions

The response matrix summary the data as follows:

West Antarctica:

VE_WA_no_DL has the following entries, [HL, AV, LAT, TIME, VAR]

HL: Lithosphere thickness; 30 km, 40 km, …, 90 km (7 entries)

AV : Asthenosphere Viscosity; $1 \times 10^{18}\ Pa\ s$, $3 \times 10^{18}\ Pa\ s$, $10 \times 10^{18}\ Pa\ s$, $30 \times 10^{18}\ Pa\ s$ (4 entries)

LAT: Latitude grid node, corresponding to file ‘Coord_Co-Latitude.mat’ (1537 entries)

TIME: Time, corresponding to file ‘Time_WA_rheo.mat’ (202 entries)

VAR: Variable type; 1: rate of radial displacement in mm/yr, 2: rate of geoid-height change in mm/yr.

The response kernels for *East Antarctica* are organized analogue, [HL, LAT, TIME, VAR]

HL: Lithosphere thickness; 150 km, 200 km (2 entries)

Note that the asthenosphere and upper mantle viscosity is constant at $5 \times 10^{20}\ Pa\ s$ and therefore has no entry.

The spectral resolution underlying these fields is spherical-harmonic cut-off degree 2048. The user should apply an adequate smoothing filter when using for inverting GRACE gravity fields. Filtered kernels are available upon request by the author.

5.6.2 *Geodesic grid*

The computation of the geodesic grid is not an original contribution of the authors, but based on the grid generator of the ICON GCM project, http://icon-downloads.zmaw.de/. For completeness, we provide the data set with disc locations based. An alternative resource for downloading geodesic grids at different resolutions in netCDF format can be found here: http://kiwi.atmos.colostate.edu/BUGS/geodesic/ .

The files format is:

vert-7.mask.cont_and_shelf.re.dat: Longitude [°], Latitude [°]

vert-7.mask.cont_and_shelf.re.proj.dat: X [km], Y [km], (projected coordinates, WGS-84, Polar Stereographic, 71°S true latitude, 0°E central longitude)

5.6.3 *Lithosphere thickness*

The thickness of the elastic lithosphere at the locations of the geodesic grid for different values of the viscosity threshold applied to the data set of Priestley & McKenzie, 2013.

lith_thresh_21.disc.txt (threshold 10^{21} Pa s, thicker lithosphere)

lith_thresh_22.disc.txt (threshold 10^{22} Pa s, lithosphere adopted in the GIA estimate)

lith_thresh_23.disc.txt (threshold 10^{23} Pa s, thinner lithosphere)

The 1175 entries correspond to the locations of the geodesic grid (Section 5.6.2).

5.6.4 *Open source code for viscoelastic modelling*

The opens source software package SELEN allows the computation of the Maxwell-viscoelastic Earth response to user-defined ice sheet evolutions, in particular also a simplified disc-load forcing as presented in this paper. The program is downloadable at: https://geodynamics.org/cig/software/selen/

6. Conclusions

In this paper, we have presented refined temporal linear trends of surface elevation, gravity field change and bedrock displacement based on Envisat/ICESat (2003-2009), GRACE (2003-2009) and GPS (1995-2013.7), respectively. In addition, we have performed forward modelling of the viscoelastic response of the solid Earth to a disc-load forcing. These response functions are particularly suited to represent the distinct geological regimes of East and West Antarctica in the joint inversion of multiple satellite data. Similarly, the functions can be applied to the other geographical regions as well. The data and code necessary to reproduce our results, or apply our approach to a different problem, is provide at www.pangea.de, https://doi.pangaea.de/10.1594/PANGAEA.875745 (follow link “View dataset as HTML”)..

We have refined surface-elevation rates for the Antarctic ice sheet for the time interval 2003-2009 by combining Envisat and ICESat altimetry data. The straightforward compositing approach performs a grid-based comparison of the noise in the elevation rates obtained from Envisat and ICESat. For large parts of the ice sheet, the elevation rate is based on ICESat data, particularly, along for the rough terrain along coast, as well as close to the Pole (polar gap of Envisat). Envisat contributes in some low-relief areas in East Antarctica and along the Antarctic Peninsula, as well as along single spurious ICESat tracks. Thus, the composite elevation rates are maximized in terms of spatial coverage and minimized in terms of the uncertainties.

The GPS processing carried out as part of the RATES and REGINA projects has produced a comprehensive data set of Antarctic 118 GPS records, which, for continuous sites, spans a longer time interval (1995-2013) than those of previous studies (Thomas et al. (2011), 1995-2011; Argus et al. (2014), 1994-2012; Martín-Español et al. (2016b), 2009-2014). The ensemble processing done for the REGINA project has allowed us to assess the contribution of systematic error sources. In addition, for sites where there is potential doubt over about the quality of the metadata or the behaviour of the site, we have adopted a 'conservative but realistic' approach to assigning new confidence limits. The screening of GPS data for outliers involved careful manual assessment, encompassing the review of measurement logs and notes on problems in the field. The data quality is reflected in the uncertainty estimates for the GPS rates, which therefore represents more reliable input data than GPS rates based on processing without manual intervention. Note, however, SMB variations might also contribute to the GPS uplift rates given that the time spans of these data vary [R2_867].

We have optimized the post-processing sequence for estimating the temporal linear trend and its uncertainty in the GRACE gravity field solutions for the region of Antarctica. In particular, we have derived optimal parameters for de-striping the monthly gravity fields over Antarctica according to Swenson & Wahr (2006). In addition, we have removed de-trended ~~interannual~~ SMB fluctuations [R1_476] from the GRACE time series, to obtain a more representative uncertainty estimate based on the post-fit RMS residual. We have included month-dependent weighting in the least-squares estimate of the gravity field rates to account for the varying quality of the monthly GRACE solutions. The optimization of the de-correlation filter of Swenson & Wahr (2006) to the signals expected in Antarctica reduced the residual uncertainty and improved the reliability of inferred mass anomalies.

With the aim of joining the multiple satellite data using the knowledge of the geophysical processes involved, we have calculated elastic and viscoelastic response functions of the solid Earth. The viscoelastic response functions represent the gravity field change and surface displacement to a disc-load forcing for a variety of Earth model parameters; particularly, ~~however,~~ values of mantle viscosity and lithosphere thickness strongly varying between the distinct geological regimes of West and East Antarctica.

In particular, we have investigated the effect of a ductile layer in the crustal lithosphere on the viscoelastic rebound signature. We show that for moderate load changes of 0.45 m/yr water-equivalent (here, applied as disc load with a radius of ca. 63 km), uplift rates reach the cm/yr level within decades assuming asthenosphere viscosities $< 10^{19}$ Pa s and lithosphere thickness < 50 km; both plausible values for parts of West Antarctica. Including a ductile layer in the crustal lithosphere further attenuates the uplift rates and localizes the deformational response. This suggests that GIA in West Antarctica may locally be a result of more recent, centennial load changes, most notably in the Amundsen Sea Embayment and in part of the Antarctic Peninsula (Nield et al. 2012~~).~~ Similar conclusion were reached by Ivins & James (2005) and Nield et al. (2014), even though it is not possible to constrain the exact timing of the load from our approach [R1_921]~~.~~

The advantage of the viscoelastic response kernels is that a meaningful ratio of rate of the gravity disturbance versus rate of the surface displacement [R1_923] is calculated for each choice of the Earth model parameters, avoiding the approximation with an average rock density (e.g. Riva et al. 2009; Gunter et al. 2014). Using the response functions allows us to reconcile GIA signatures with measurements of large bedrock uplift and small gravity field increase in the Amundsen Sea Embayment, associated with weak Earth structures. Clearly, the response functions adopted here represent only the viscoelastic equilibrium state and, thus, are considered only an intermediate step to full dynamic modelling of the GIA response. Nevertheless, this approximation represents a significant improvement of other joint inversion methods, as it bases the joint inversion on physically meaningful response kernels. With extra data on the past ice evolution, such as Paleo thickness rates, our approach can be expanded to address the temporal evolution as well.

In the succeeding paper REGINA part II (Sasgen et al. 2017~~submitted~~), we perform the joint inversion for present-day ice-mass changes and GIA in Antarctica, based on the input data sets and viscoelastic response functions presented here. We validate our results using forward-modelling results and other empirical models, and show the impact on CryoSat-2 volume and GRACE mass balances, respectively. Note, however, that the post-processing methods and viscoelastic functions presented here are applicable also to other geographical regions with superimposed present-day mass change and GIA signatures.

7. Data Availability

The altimetry, gravimetry, GPS and viscoelastic modelling data used in this project are available at https://doi.pangaea.de/10.1594/PANGAEA.875745 in the www.pangea.de archive. The data description and user documentation are given for each data type within the respective subsection of this paper (Sections 2 to 5).

Author Contribution

Ingo Sasgen conceived, managed and summarized this study with support of Mark R. Drinkwater. Alba Martín-Español, Bert Wouters and Jonathan L. Bamber performed the altimetry analysis. Alexander Horvath, Martin Horwath and Roland Pail undertook the gravity field analysis, with contributions from Ingo Sasgen. Elizabeth J. Petrie and Peter J. Clarke ~~analysis~~ analyzed and clustered the GPS data with critical input from Terry Wilson. Volker Klemann and Hannes Konrad performed the viscoelastic modelling, with contributions from Ingo Sasgen. All authors were involved in writing and reviewing this manuscript.

Competing Interest

The authors declare that they have no conflict of interest.

Acknowledgements

The www.regina-science.eu work was enabled through CryoSat+ Cryosphere study funding from the Support To Science Element (STSE) of the European Space Agency (ESA) Earth Observation Envelope Programme. I.S. acknowledges additional funding through the German Academic Exchange Services (DAAD) and DFG grant SA1734/4-1 and P.J.C. and E.J.P. from UK NERC grant NE/I027401/1 (RATES project). We thank Thomas Flament and Frederique Rémy for the Envisat data and Veit Helm for providing the AWI L2 CryoSat-2 re-tracked and corrected elevation measurements. The GPS data used was mainly downloaded from publically available archives. We acknowledge work done by the International GNSS Service (Dow et al., 2009), UNAVCO and the Scientific Committee on Antarctic Research in maintaining such archives, together with the efforts of all the GPS site operators in collecting and making available the data, a particularly challenging task in Antarctica (see Table S2 for more information on individual sources).

A.1 ICESat campaigns and operation periods

Table A.1. ICESat 633 Level 2 data for the time span February 2003 until October 2009 used in this study.

Start Date	End Date	Days in Operation	Laser Identifier
20/02/2003	29/03/2003	38	1AB
25/09/2003	19/11/2003	55	2A
17/02/2004	21/03/2004	34	2B
18/05/2004	21/06/2004	35	2C
03/10/2004	08/11/2004	37	3A
17/02/2005	24/03/2005	36	3B
20/05/2005	23/06/2005	35	3C
21/10/2005	24/11/2005	35	3D
22/02/2006	28/03/2006	34	3E
24/05/2006	26/06/2006	33	3F
25/10/2006	27/11/2006	34	3G
12/03/2007	14/04/2007	34	3H
02/10/2007	05/11/2007	37	3I
17/02/2008	21/03/2008	34	3J
04/10/2008	19/10/2008	16	3K
25/11/2008	17/12/2008	23	2D
09/03/2009	11/04/2009	34	2E
30/09/2009	11/10/2009	12	2F

A.2 Firn compaction and SMB corrections

We apply rates of firn compaction, h_{comp}, using output of the firn compaction model provided by Ligtenberg (2011), which is driven by RACMO2/ANT (Lenaerts 2010). However,

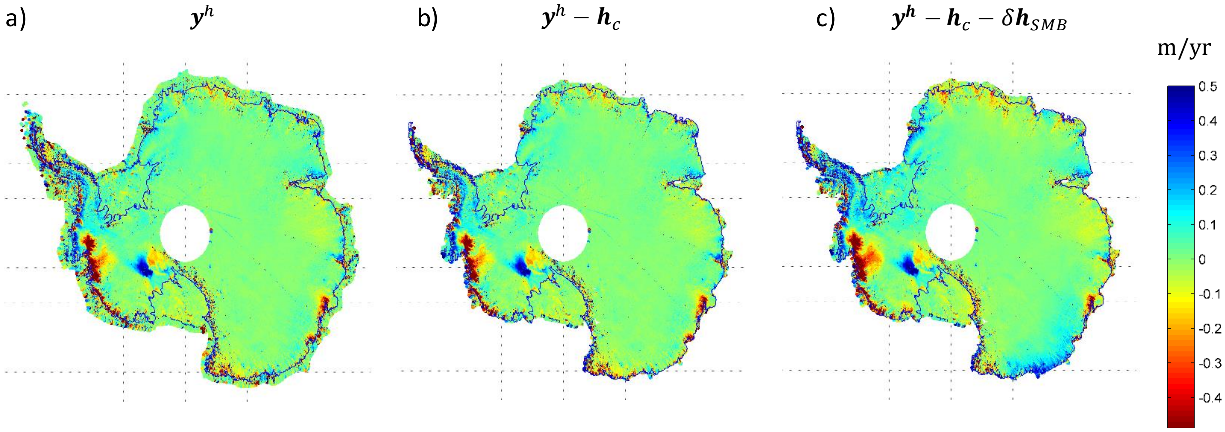

Figure A.1 Rate of elevation change y^h (m/yr), derived from a) ICESat/Envisat initial data, b) ICESat/Envisat minus firn ~~compaction~~ compaction h_{comp}, and c) ICESat/Envisat minus firn compaction h_{comp} and modelled SMB anomalies δh_{SMB}.

we do not apply a correction for anomalies in the surface-mass balance (SMB), δh_{SMB}, as e.g. undertaken by Gunter et al. (2014), due to the problem of defining an adequate reference period for the ice sheet. The impact of each correction is shown in Fig. A.1. Note that annual anomalies of the firn densification for the years 2003-2013 are available in the data archive http://hs.pangaea.de/model/Sasgen-etal_2017/Ice_sheet_topographic_change.zip

1008 *A.3 Flowchart of estimation process for Antarctic GPS site time series.*

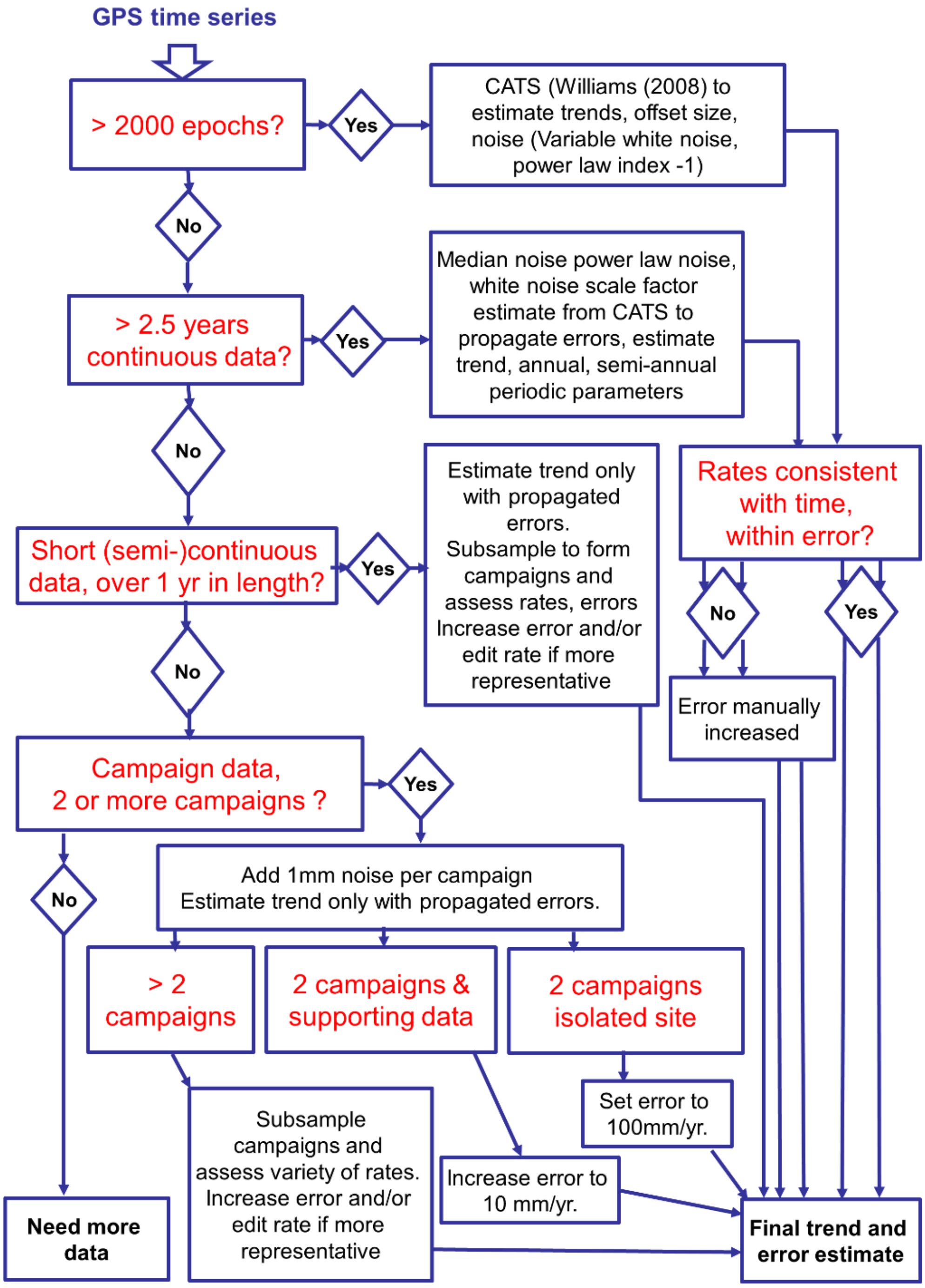

Figure A.2 Flowchart showing the estimation process for the temporal linear trends of the bedrock for Antarctic GPS site timeseries. After Petrie et al. (2016) (SCAR poster)

A.4 Uplift rates at all GPS site used in this study

Table A.2 GPS uplift rates for this study. The columns are: site name, estimated uplift rate y^u (mm/yr), estimated uncertainty σ^u (mm/yr), rate method, uncertainty method, approx latitude (dec. degrees), approximately~~x.~~ longitude (dec. degrees). Methods are: cats: estimated by the CATS noise analysis software ('cats'), median uncertainty from CATS sites propagated ('prop'), manual intervention in rate due to potential systematic uncertainties ('rman') and manual intervention in uncertainties due to potential systematic errors

Site name	y^u	σ^u	Method y^u	Method σ^u	Lat. (°)	Lon. (°)	Doi/ data source or description
aboa	**0.6**	0.5	cats	cats	-73.04	-13.41	Finnish Geodetic Institute
brip	**1.4**	0.7	cats	cats	-75.80	158.47	doi:10.7283/T5W09473
buri	**2.3**	0.7	cats	cats	-79.15	155.89	doi:10.7283/T5RB72W7
cas1	**1.5**	0.2	cats	cats	-66.28	110.52	IGS: Dow et al. (2009)
cote	**1.4**	0.7	cats	cats	-77.81	162.00	doi:10.7283/T5GT5KGN
crar	**0.7**	0.4	cats	cats	-77.85	166.67	UNAVCO*
dav1	**-1.6**	0.6	rman	eman	-68.58	77.97	IGS: Dow et al. (2009)
dum1	**-0.3**	0.3	cats	cats	-66.67	140.00	IGS: Dow et al. (2009)
flm5	**2.0**	0.6	cats	cats	-77.53	160.27	doi:10.7283/T5V40SH6
ftp4	**1.9**	0.6	cats	cats	-78.93	162.56	doi:10.7283/T5B27SKD
maw1	**-0.4**	0.2	cats	cats	-67.60	62.87	IGS: Dow et al. (2009)
mcm4	**0.8**	0.2	cats	cats	-77.84	166.67	IGS: Dow et al. (2009)
min0	**2.0**	0.8	cats	cats	-78.65	167.16	doi:10.7283/T5TM78BX
ohi2	**3.4**	2.0	cats	eman	-63.32	-57.90	IGS: Dow et al. (2009)
palm	**4.8**	3.0	cats	eman	-64.78	-64.05	IGS: Dow et al. (2009)
ramg	**2.4**	0.8	cats	cats	-84.34	178.05	doi:10.7283/T51N7ZFR
rob4	**1.1**	0.5	cats	cats	-77.03	163.19	doi:10.7283/T5NC5ZG8
sctb	**0.9**	0.5	cats	cats	-77.85	166.76	doi:10.7283/T5CF9N6P
syog	**1.1**	0.2	cats	cats	-69.01	39.58	IGS: Dow et al. (2009)
tnb1	**0.1**	0.5	cats	cats	-74.70	164.10	Dubbini et al. (2010)
vesl	**0.4**	0.3	cats	cats	-71.67	-2.84	IGS: Dow et al. (2009)
a351	**-0.9**	1.8	prop	eman	-72.91	74.91	Geoscience Australia**
a368	**-0.2**	1.2	prop	eman	-74.29	66.79	Geoscience Australia**
arct	**-0.1**	4.4	prop	eman	-80.04	-80.56	SCARP***
art1	**-3.1**	10.0	prop	eman	-62.18	-58.90	Dietrich et al. (2004)
back	**16.8**	5.0	prop	eman	-74.43	-102.48	doi:10.7283/T5D21VWM
bean	**2.1**	4.3	rman	eman	-75.96	-69.30	doi:10.7283/T55Q4T6R

belg	**-1.4**	0.7	prop	prop	-77.87	-34.63	Dietrich et al. (2004)
benn	**9.3**	1.9	prop	prop	-84.79	-116.46	doi:10.7283/T5891447
berp	**25.2**	0.7	prop	prop	-74.55	-111.88	doi:10.7283/T54J0CC2
bhil	**2.9**	4.4	rman	eman	-66.25	100.60	Geoscience Australia**
bren	**3.1**	1.1	rman	eman	-72.67	-63.03	doi:10.7283/T52V2D7X
capf	**4.0**	1.4	rman	eman	-66.01	-60.56	doi:10.7283/T5XP736P
cjam	**-2.3**	100.0	prop	eman	-63.10	-62.72	SCARP***
clrk	**3.6**	1.4	prop	prop	-77.34	-141.87	doi:10.7283/T5MK6B6C
coat	**-0.1**	7.3	prop	eman	-77.81	162.00	Raymond et al. (2004)
crdi	**2.1**	0.6	prop	prop	-82.86	-53.20	doi:10.7283/T5C24TQS
cwal	**0.4**	100.0	prop	eman	-63.25	-62.18	SCARP***
dal1	**4.9**	34.4	prop	eman	-62.24	-58.68	Dietrich et al. (2004)
dall	**-17.0**	100.0	prop	eman	-62.24	-58.66	Dietrich et al. (2004)
devi	**1.9**	1.0	prop	prop	-81.48	161.98	doi:10.7283/T57942Z0
dupt	**11.5**	1.1	prop	prop	-64.81	-62.82	doi:10.7283/T5KD1W62
eacf	**-4.8**	15.0	rman	eman	-62.08	-58.39	Brazil
elph	**6.3**	100.0	prop	eman	-61.22	-55.14	SCARP***
esp1	**5.6**	100.0	prop	eman	-63.40	-57.00	Dietrich et al. (2004)
fall	**4.8**	1.3	prop	prop	-85.31	-143.63	doi:10.7283/T53J3B84
ferr	**-5.5**	31.0	rman	eman	-62.09	-58.39	Dietrich et al. (2004)
fie0	**-0.9**	1.9	prop	prop	-76.14	168.42	doi:10.7283/T5KK993F
flm2	**3.8**	11.7	rman	eman	-77.53	160.27	doi:10.7283/T53T9FHJ
fonp	**13.5**	1.8	prop	prop	-65.25	-61.65	doi:10.7283/T5668BG6
for1	**-0.2**	2.9	prop	eman	-70.78	11.83	Dietrich et al. (2004)
for2	**-0.3**	2.7	prop	eman	-70.77	11.84	Dietrich et al. (2004)
fos1	**3.1**	1.3	prop	eman	-71.31	-68.32	doi:10.7283/T54T6GF7
frei	**-4.4**	0.7	prop	prop	-62.19	-58.98	Bevis et al. (2009)
ftp1	**-2.2**	3.4	prop	eman	-78.93	162.56	doi:10.7283/T53T9FHJ
gmez	**1.5**	4.8	rman	eman	-73.89	-68.54	doi:10.7283/T58G8HT4
grw1	**-7.0**	8.6	prop	eman	-62.22	-58.96	Dietrich et al. (2004)
haa1	**3.9**	100.0	prop	eman	-77.04	-78.29	British Antarctic Survey
haag	**6.1**	1.1	rman	eman	-77.04	-78.29	doi:10.7283/T5FT8JB8
howe	**0.6**	1.1	rman	eman	-87.42	-149.43	doi:10.7283/T5ZW1J65
hown	**3.9**	0.8	prop	prop	-77.53	-86.77	doi:10.7283/T56971WH
hton	**4.8**	3.7	prop	eman	-74.08	-61.73	doi:10.7283/T5222RV6
hugo	**0.9**	1.3	prop	prop	-64.96	-65.67	doi:10.7283/T5FQ9TW3
iggy	**2.3**	1.1	prop	eman	-83.31	156.25	doi:10.7283/T5QC01T9
jnsn	**4.0**	1.7	prop	prop	-73.08	-66.10	doi:10.7283/T5SJ1HP1
lntk	**4.6**	3.1	rman	eman	-74.84	-73.90	doi:10.7283/T5J1017P
lply	**2.0**	8.1	rman	eman	-73.11	-90.30	doi:10.7283/T5DV1H50
lwn0	**2.1**	1.0	prop	prop	-81.35	152.73	doi:10.7283/T5T43RD8
mait	**0.4**	1.1	rman	eman	-70.77	11.74	Dietrich et al. (2004)
mar1	**7.1**	10.0	prop	eman	-64.24	-56.66	Dietrich et al. (2004)
mbl1	**2.5**	3.0	prop	eman	-78.03	-155.02	Donnellan & Luyendyk (2004) + doi:10.7283/T5CJ8BS7

mbl2	**2.3**	10.0	prop	eman	-76.32	-144.31	Donnellan & Luyendyk (2004)
mbl3	**1.3**	17.9	rman	eman	-77.34	-141.87	Donnellan & Luyendyk (2004)
mcar	**3.7**	1.4	prop	prop	-76.32	-144.30	doi:10.7283/T55D8Q41
mirn	**24.4**	100.0	prop	eman	-66.55	93.01	SCAR
mkib	**4.7**	2.6	rman	eman	-75.28	-65.60	doi:10.7283/T5D798HD
mtcx	**-3.8**	10.0	prop	eman	-78.52	162.53	Raymond et al. (2004)
ohg1	**4.5**	10.0	prop	eman	-63.32	-57.90	Dietrich et al. (2004)
ohig	**4.0**	0.7	prop	prop	-63.32	-57.90	Former IGS: Dow et al. (2009)
pal1	**8.1**	10.0	prop	eman	-64.77	-64.05	Dietrich et al. (2004)
patn	**4.8**	0.7	prop	prop	-78.03	-155.02	doi:10.7283/T5PC30PX
pece	**0.7**	4.2	prop	eman	-85.61	-68.56	doi:10.7283/T5930RG1
pra1	**4.2**	10.0	prop	eman	-62.48	-59.65	Dietrich et al. (2004)
prat	**-9.6**	100.0	prop	eman	-62.48	-59.65	doi:10.7283/T5M32T21, doi:10.7283/T5K35RZP
prtt	**-5.0**	100.0	prop	eman	-62.48	-59.67	SCARP***
reyj	**151.3**	300.0	prop	eman	-62.20	-58.98	doi:10.7283/T5M32T21, doi:10.7283/T5K35RZP
rob1	**5.4**	5.1	prop	eman	-77.03	163.19	doi:10.7283/T5057D6V, doi:10.7283/T53T9FHJ
robi	**8.7**	1.5	prop	prop	-65.25	-59.44	Nield et al. (2014)
rot1	**6.5**	10.0	prop	eman	-67.57	-68.13	SCAR
rotb	**5.0**	0.4	prop	prop	-67.57	-68.13	doi:10.7283/T56M34Z7
roth	**5.5**	1.4	prop	prop	-67.57	-68.13	IGS: Dow et al. (2009)
sdly	**-0.3**	1.4	prop	prop	-77.14	-125.97	doi:10.7283/T5S46Q7F
sig1	**23.0**	100.0	prop	eman	-60.71	-45.59	Dietrich et al. (2004)
smr1	**0.5**	10.0	prop	eman	-68.13	-67.10	Dietrich et al. (2004)
smrt	**1.2**	0.9	prop	prop	-68.13	-67.10	Alfred Wegener Institute / Instituto Antartico Argentina
sppt	**12.9**	100.0	prop	eman	-64.29	-61.05	Bevis et al. (2009)
sugg	**4.7**	1.3	rman	eman	-75.28	-72.18	doi:10.7283/T5CV4G1M
svea	**1.3**	1.1	prop	prop	-74.58	-11.23	Sjoberg et al. (2011)
thur	**-1.2**	2.5	rman	eman	-72.53	-97.56	doi:10.7283/T5862DRZ
tomo	**47.7**	20.3	rman	eman	-75.80	-114.66	doi:10.7283/T5BZ64B0
trve	**2.5**	5.6	rman	eman	-69.99	-67.55	doi:10.7283/T5NS0RZ9
ver1	**0.3**	100.0	prop	eman	-65.25	-64.26	SCAR
ver3	**-6.2**	100.0	prop	eman	-65.25	-64.26	SCAR
vnad	**4.4**	1.1	prop	prop	-65.25	-64.25	doi:10.7283/T52F7KQ1
w01b	**1.4**	10.0	prop	eman	-87.42	-149.44	doi:10.7283/T5445JTQ doi:10.7283/T50C4T3D
w02b	**2.3**	10.0	prop	eman	-85.61	-68.56	
w03a	**-1.4**	10.0	prop	eman	-81.58	-28.40	
w03b	**1.7**	10.0	prop	eman	-81.58	-28.40	
w05a	**2.3**	10.0	prop	eman	-80.04	-80.56	doi:10.7283/T57W69HP doi:10.7283/T50C4T3D
w05b	**7.4**	10.0	prop	eman	-80.04	-80.56	

w06a	**-2.2**	100.0	prop	eman	-79.63	-91.28	
w07a	**3.3**	100.0	prop	eman	-80.32	-81.43	
w08a	**-1.5**	100.0	prop	eman	-75.28	-72.18	
w09a	**2.2**	100.0	prop	eman	-82.68	-104.40	
wasa	**0.6**	3.2	prop	eman	-73.04	-13.41	Sweden
whn0	**2.2**	0.9	prop	prop	-79.85	154.22	doi:10.7283/T5R49P2M
whtm	**7.7**	0.8	prop	prop	-82.68	-104.39	doi:10.7283/T5ZP44DZ
wiln	**4.9**	0.9	prop	prop	-80.04	-80.56	doi:10.7283/T53F4MX9

*https://www.unavco.org/projects/project-support/polar/geodetic/benchmarks/sites/crar.html (accessed 1 June 2017)

**Geoscience Australia GNSS archive at ftp://ftp.ga.gov.au/geodesy-outgoing/gnss/ as of 1 June 2017. See also Brown, N. and Woods, A., 2008. Antarctic Geodesy 2006 – 2007 Field Report. Geoscience Australia, Record 2009/32. 77pp.

*** SCARP Campaign datasets, doi:10.7283/T5T151QB, doi:10.7283/T59P2ZZD, doi:10.7283/T5K35RZP. Also see https://gcmd.nasa.gov/records/GCMD_JCADM_USA_SCARP.html

Table A.3. Comparison of 'prop,eman' GPS uplift rates for this study with rates from other studies.

	REGINA		Thomas et al. 2011		Argus et al. (2014)		Wolstencroft et al. (2015)	
	y^u	σ^u	y^u	σ^u	y^u	σ^u	y^u	σ^u
a351	**-0.9**	1.8	**0.8**	1.3	**1.1**	3.5		
a368	**-0.2**	1.2	**0.4**	1.0				
for1	**-0.2**	2.9	**-1.4**	0.8				
for2	**-0.3**	2.7	**2.1**	0.9				
fos1	**3.1**	1.3	**2.1**	0.4	**2.9**	1.2	**3.9**	1.1
ftp1	**-2.2**	3.4	**2.1**	2.8				
hton	**4.8**	3.7						
mbl1	**2.5**	3.0	**0.6**	1.5				
mbl2	**2.3**	10	**0.2**	4.1			**6.4**	0.9
rob1	**5.4**	5.1	**7.5**	2.6				
w01a(-howe)	**-0.3**	10	**-2.5**	1.7	**0.9**	1.2		
w01b	**1.4**	10	**-3.1**	1.7				
w02a(-pece)	**0.3**	10	**2.8**	1.2	**–1.2**	1.9		
w02b	**2.3**	10	**0.5**	1.9				
w03a	**-1.4**	10	**-3.2**	1.8	**–1.1**	2.4		
w03b	**1.7**	10	**-1.7**	1.8				
w04a	**3.7**	100	**3.0**	1.1				
w05a	**2.3**	10	**3.5**	2.0				
w05b	**7.4**	10	**5.3**	1.2				
w06a	**-2.2**	100	**-2.2**	2.4	**–4.7**	4.4		
w07a	**3.3**	100	**3.3**	2.1	**4.6**	3.1		
w08a(b/sugg)	**-1.5**	100	**1.3**	1.3				
w09a	**2.2**	100	**4.5**	2.6				

A.5 Choice of GRACE cut-off degree and biasing

In this study, we identify GRACE coefficients of CSR RL05 up to-degree and order 50 appropriate to yield the most robust gravity field rates over Antarctica. Figure A.3 provides another indication based on the degree-power spectrum of the geoid rates. It is visible that GFZ RL05 and CSR RL05 are very similar up to degree and order 50, where the power spectra show minima. For higher degrees, however, the power of the gravity field recovered with GRACE

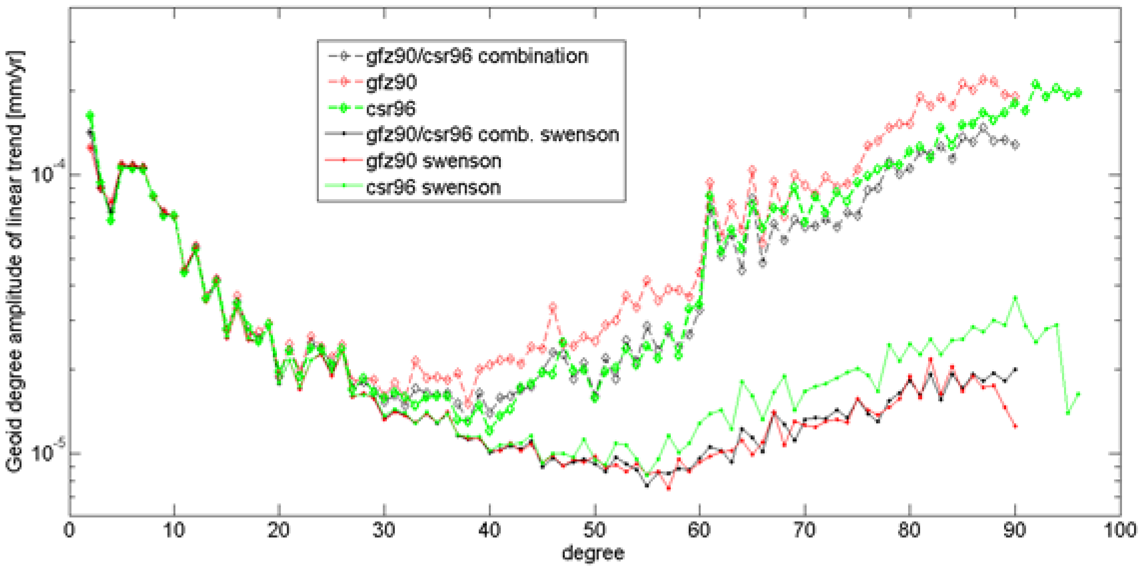

Figure A.3: Degree-amplitude spectrum of the rate of geoid-height change (mm/yr) for unfiltered (diamond-dashed lines) and for Swenson-filtered (solid lines) solutions. Red: GFZ; green: CSR; black combination of GFZ and CSR with equal weights.

increases due to increasing noise, for the unfiltered coefficients particularly faster for GFZ RL05 than for CSR RL05.

The filtering of the GRACE gravity fields was optimized for reducing noise over Antarctica. The effect on the RMS uncertainties is shown in Fig. 3. Additionally, Fig. A.4

presents the difference of between the GRACE rates filtered only with a Gaussian smoothing filter of 200 km, and additionally with the optimized Swenson filter. It is visible that the differences in the rate of geoid-height change and the associated rate of equivalent water-height change, respectively, show a stripe-like noise pattern. This suggests that the de-striping is superior over conventional Gaussian smoothing, even at high latitudes, where GRACE ground-track spacing is very dense. It is also important to note that the filter does not introduce any magnitude bias, or changes the spectral content of the gravity field rates, which is important when applying only Gaussian smoothing of 200 km (without Swenson filtering) to the altimetry data set and response kernels.

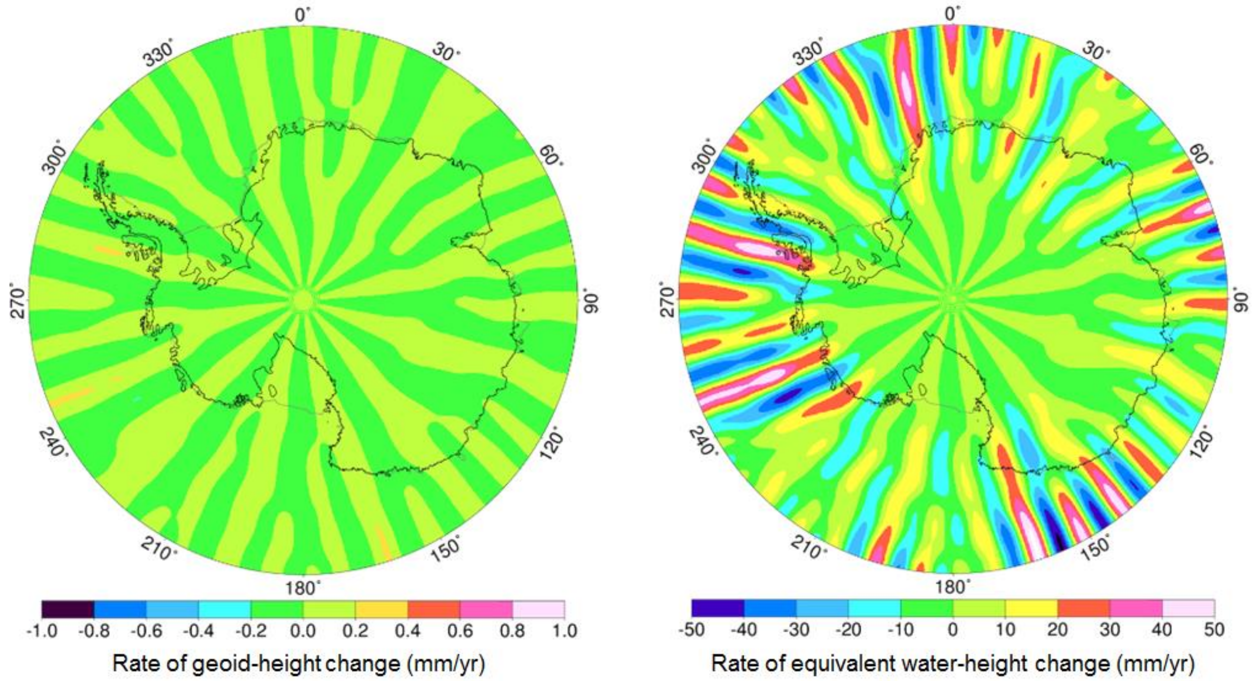

Figure A.4: Spatial rate of geoid-height change (left) and rate of equivalent water-height change (right) (mm/yr) for the difference between the GRACE trends processed by Gaussian smoothing of 200 km and the optimal Swenson filter & Gaussian smoothing. The solutions are CSR RL05, the spherical-harmonic cut-off degree is 50.

A.6 Evaluation of assumption of viscoelastic equilibrium state

The viscoelastic response kernels employed (Section 5) describe the viscoelastic equilibrium state for the forcing with a disc load of constant radius and constant rate of mass increase (likewise mass loss). We neglect transitional changes of the solid Earth for load changes that have not reached the equilibrium state in terms of geoid-height change and surface displacement. Although, the deformation and gravity signature in equilibrium eventually only depends on the lithosphere thickness, the time to reach the equilibrium is controlled by the viscosity parameters chosen. Fig. A.5 shows the evolution of the standardized ratio of the geoid-

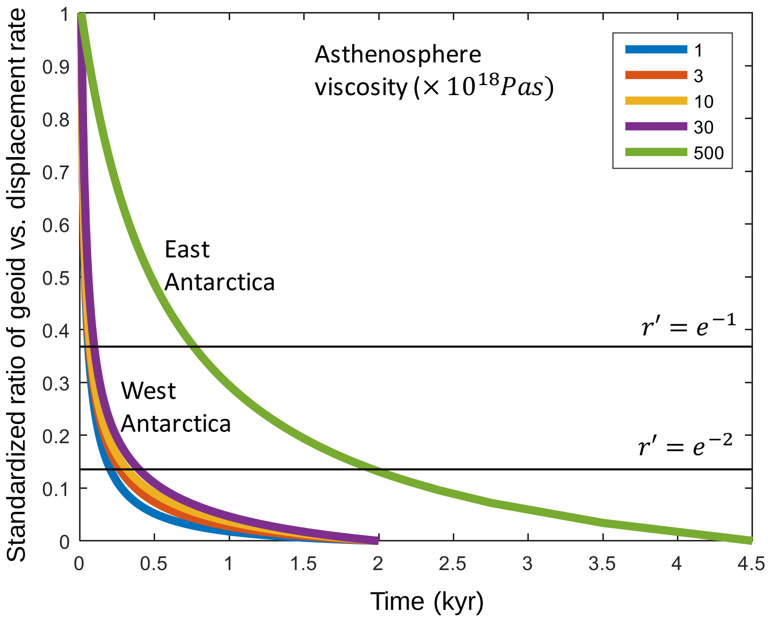

Figure A.5: Standardized ratio of the rate of geoid-height change versus the rate of radial displacement for different values of the asthenosphere viscosity. Note that the ratio is calculated at the load center.

height change vs. surface displacement over time, calculated as $r' = [r(t) - r(t = t_{tmax})]/\max[r(t) - r(t = t_{tmax})]$, where $r = y^g(t)/y^u(t)$ is evaluated at the load centre. It is visible that for the weaker West Antarctic rheology (asthenosphere viscosity between 1×10^{18} Pa s and 3×10^{19} Pa s) r' falls to 1/e² within the 500 yr. For East Antarctica (1×10^{20}Pas), $r' = e^{-2}$ is reached within 2 kyrs. With this quasi-stationary solution approach, the inference on the timing of the past ice mass change is limited to an upper limit in terms of magnitude, and a lower limit in terms of load duration; a similar ratio is achieved by a thinner lithosphere thickness, which has not reached viscoelastic equilibrium state, and earlier load changes are fully relaxed, respectively.

A.7 *Assessment of SMB fluctuations on GPS uplift rates* [R2_867]

We assess the impact of SMB fluctuations on the uplift rate at the GPS station locations

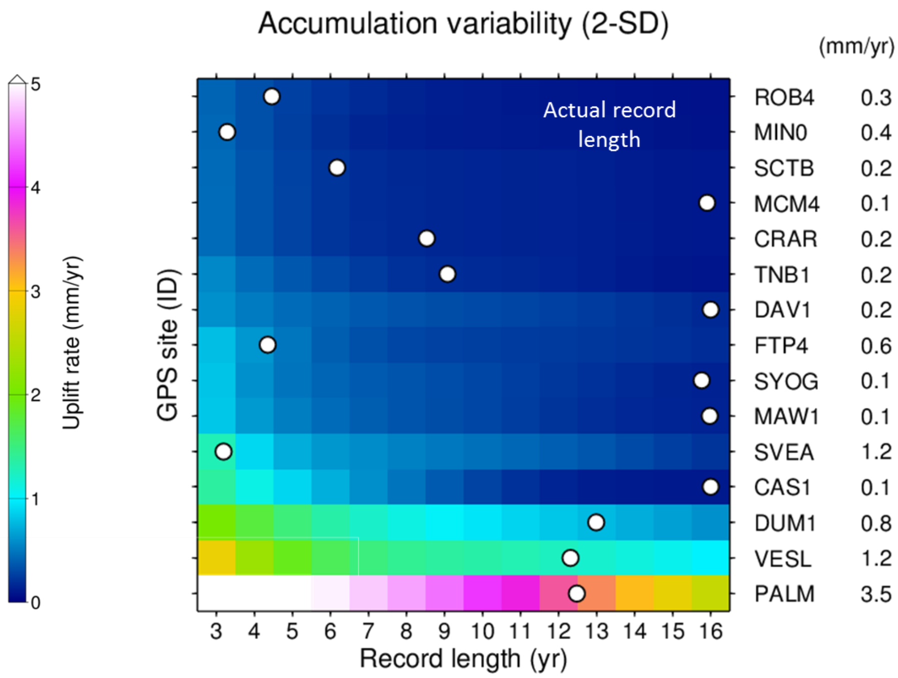

Figure A,6: Standard deviation (2-sigma) of the uplift rates caused by accumulation variability for different GPS stations and time periods. It is visible that the uncertainty decreases with record length; for most regions, trend uncertainties are below 0.4 mm/yr for the actual GPS record length.

using the modelled SMB of RACMO2 for the years 1979-2010. We compute the elastic deformation related to cumulative monthly SMB, de-trended for the entire simulation period 1979-2010. We then estimate the temporal linear trends at the GPS station locations for a moving window of varying width from 3 to 16 years. Then, for each window width, we estimate the standard deviation of the apparent trend induced by SMB for selected stations (Fig. A.7). Typically, the uncertainty of uplift rate due to SMB variability is below 0.4 mm/yr for the actual GPS record length. An exception is PALM, which is located on the Antarctica Peninsula - a region with annual accumulation of up to 4 m/yr equivalent water height. Here, even after 12 years of measurements, GPS uplift rates are likely to contain accumulation signals of 4 mm/yr. A similar effect of the SMB fluctuations is expected at VESL.

~~A.7~~A.8 Load evolution for the viscoelastic response functions [R2_867]

The load increases, with a fixed radius, at a constant rate of *ca.* 5.6 Gt/yr until an approximate equilibrium state is reached; 2 kyr for West Antarctica and 15 kyr for East Antarctica (Fig. A.7). Then the load is applied without a change to obtain the purely viscoelastic response of the Earth model, i.e. without direct gravitational attraction of the load and the instantaneous elastic response. The associated Earth response constitutes the viscoelastic response functions adopted in the joint inversion.

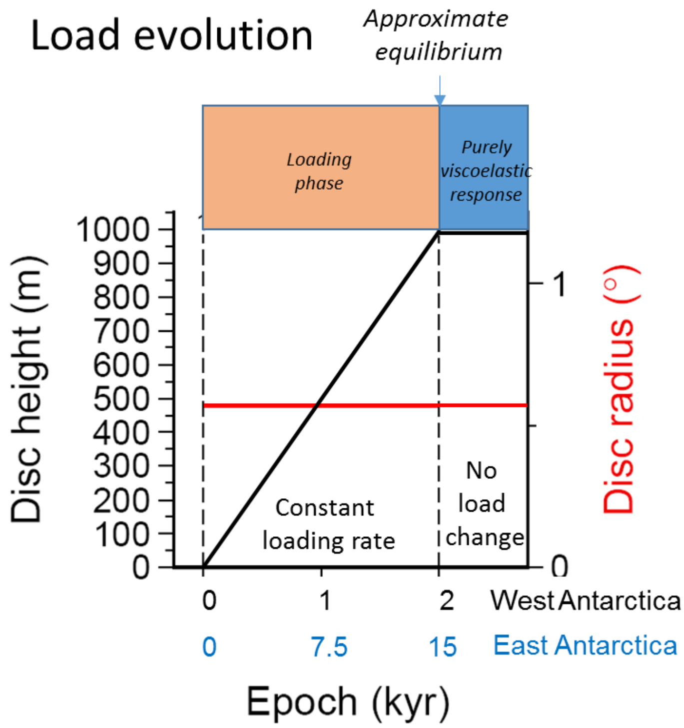

[R2_1014] Figure A,7: Load function applied to obtain the viscoelastic response functions.

REFERENCES

An, M., Wiens, D. A., Zhao, Y., Feng, M., Nyblade, A. A., Kanao, M., Li, Y., Maggi, A. & Lévêque, J. J. (2015). S-velocity model and inferred Moho topography beneath the Antarctic Plate from Rayleigh waves. *J. Geophys. Res.*: Solid Earth, 120(1), 359-383.

Argus, D. F., Peltier, W. R., Drummond, R., & Moore, A. W. (2014). The Antarctica component of postglacial rebound model ICE-6G_C (VM5a) based on GPS positioning, exposure age dating of ice thicknesses, and relative sea level histories. *Geophys. J. Int.*, 198(1), 537-563.

Bentley, M. J., Cofaigh, C. Ó., Anderson, J. B., Conway, H., Davies, B., Graham, A. G., & others (2014). A community-based geological reconstruction of Antarctic Ice Sheet deglaciation since the Last Glacial Maximum. *Quat. Sci. Rev.*, 100, 1-9.

Bettadpur, S. (2012). Gravity Recovery and Climate Experiment UTCSR level-2 processing standards document. University of Texas at Austin, *GRACE Doc*, 327742, 16.

Bevis, M., Kendrick, E., Smalley, R., Dalziel, I., Caccamise, D., Sasgen, I., Helsen, M., Taylor, F. W., Zhou, H., Brown, A., Raleigh, D., Willis, M., Wilson, T. & Konfal, S. (2009). Geodetic measurements of vertical crustal velocity in West Antarctica and the implications for ice mass balance. Geochemistry, Geophysics, Geosystems, 10(10). doi: 10.1029/2009GC002642

Borsa, A. A., Moholdt, G., Fricker, H. A., & Brunt, K. M. (2013). A range correction for ICESat and its potential impact on ice sheet mass balance studies. *The Cryosphere Discuss.*, 7, 4287-4319.

Brenner, A. C., DiMarzio, J. P., & Zwally, H. J. (2007). Precision and accuracy of satellite radar and laser altimeter data over the continental ice sheets. *IEEE Trans. Geosci. Remote Sens.*, 45(2), 321-331.

Chambers, D. P., Bonin, J. A. (2012). Evaluation of Release-05 GRACE time-variable gravity coefficients over the ocean. *Ocean Sci.*, 8, 859-868, 2012

Cheng, M., Tapley, B. D., & Ries, J. C. (2013). Deceleration in the Earth's oblateness. *J. Geophys. Res.*: *Solid Earth*, 118(2), 740-747.

Dahle, C. (2013). GFZ GRACE level-2 processing standards document for level-2 product release 0005. *Deutsches GeoForschungsZentrum GFZ*, http://dx.doi.org/10.2312/GFZ.b103-1202-25.

Dobslaw, H.; Flechtner, F.; Bergmann-Wolf, I.; Dahle, Ch.; Dill, R.; Esselborn, S.; Sasgen, I.; Thomas, M. (2013): Simulating high-frequency atmosphere-ocean mass variability for de-aliasing of satellite gravity observations: AOD1B RL05. *J. Geophys. Res.*, doi: 10.1002/jgrc.20271.

Dow, J.; Neilan, R; & Rizos C. (2009). The International GNSS Service in a changing landscape of Global Navigation Satellite Systems. *Journal of Geodesy*, 83(3), 191-198.

Duan, X. J., Guo, J. Y., Shum, C. K., & Van Der Wal, W. (2009). On the postprocessing removal of correlated errors in GRACE temporal gravity field solutions. Journal of Geodesy, 83(11), 1095-1106.

Dubbini, M., Cianfarra, P., Casula, G., Capra, A. & Salvini, F. (2010). Active tectonics in northern Victoria Land (Antarctica) inferred from the integration of GPS data and geologic setting. *J. Geophys. Res.: Solid Earth*, 115.

Dziewonski, A. M., & Anderson, D. L. (1981). Preliminary reference Earth model. *Phys. Earth Planet. Inter.*, 25(4), 297-356.

Flament, T., & Rémy, F. (2012). Dynamic thinning of Antarctic glaciers from along-track repeat radar altimetry. *J. Glaciol.,* 58(211), 830-840.

Groh, A., Ewert, H., Scheinert, M., Fritsche, M., Rülke, A., Richter, A., Rosenau, R. & Dietrich, R. (2012). An investigation of Glacial Isostatic Adjustment over the Amundsen Sea sector, West Antarctica. Global and Planetary Change, 98–99(0), 45-53. doi: 10.1016/j.gloplacha.2012.08.001

Gunter, B. C., Didova, O., Riva, R. E. M., Ligtenberg, S. R. M., Lenaerts, J. T. M., King, M. A., van den Broeke, M. & Urban, T. (2014). Empirical estimation of present-day Antarctic glacial isostatic adjustment and ice mass change. *The Cryosphere*, 8(2), 743-760

Heeszel, D. S., Wiens, D. A., Anandakrishnan, S., Aster, R. C., Dalziel, I. W., Huerta, A. D., Nyblase, A. A., Wilson, T. J. & Winberry, P. (2016). Upper mantle structure of central and West Antarctica from array analysis of Rayleigh wave phase velocities. *J. Geophys. Res.*: *Solid Earth*, doi: 10.1002/2015JB012616.

Heiskanen, W. A., & Moritz, H. (1967). Physical geodesy. *Bulletin Géodésique* (1946-1975), 86(1), 491-492.

Hofton, M. A., Luthcke, S. B., & Blair, J. B. (2013). Estimation of ICESat intercampaign elevation biases from comparison of lidar data in East Antarctica. *Geophys. Res. Lett.*, 40(21), 5698-5703.

Horwath, M., Legrésy, B., Rémy, F., Blarel, F., & Lemoine, J. M. (2012). Consistent patterns of Antarctic ice sheet interannual variations from ENVISAT radar altimetry and GRACE satellite gravimetry. *Geophys. J. Int.*, 189(2), 863-876.

Howat, I. M., Smith, B. E., Joughin, I., & Scambos, T. A. (2008). Rates of southeast Greenland ice volume loss from combined ICESat and ASTER observations. *Geophys. Res. Lett.*, 35(17), L17505.

Hurkmans, R. T. W. L., Bamber, J. L., Sørensen, L. S., Joughin, I. R., Davis, C. H., & Krabill, W. B. (2012). Spatiotemporal interpolation of elevation changes derived from satellite altimetry for Jakobshavn Isbræ, Greenland. *J. Geophys. Res.*: *Earth Surface*, 117(F3).

Ivins, E. R., & James, T. S. (2005). Antarctic glacial isostatic adjustment: a new assessment. *Antarct. Sci.*, 17(04), 541-553.

Konrad, H., Sasgen, I., Pollard, D., & Klemann, V. (2015). Potential of the Solid-Earth response for limiting long-term West Antarctic Ice Sheet retreat in a warming climate. *Earth Planet. Sci. Lett.*, 432, 254-264.

Lenaerts, J. T. M., den Broeke, M. R., Berg, W. J., Meijgaard, E., & Kuipers Munneke, P. (2012). A new, high-resolution surface mass balance map of Antarctica (1979–2010) based on regional atmospheric climate modeling. *Geophys. Res. Lett.*, 39(4).

Ligtenberg, S. R. M., Heilsen, M. M., & van de Broeke, M. R. (2011). An improved semi-empirical model for the densification of Antarctic firn. *The Cryosphere*, 5(4), 809-819.

Martinec, Z. (2000). Spectral–finite element approach to three-dimensional viscoelastic relaxation in a spherical earth. *Geophys. J. Int.*, 142(1), 117-141.

Martín-Español, A., Zammit-Mangion, A., Clarke, P. J., Flament, T., Helm, V. , King, M. A. Luthcke, S. B., Petrie, E., Rémy, F., Schön, N. et al. (2016a), Spatial and temporal Antarctic Ice Sheet mass trends, glacio-isostatic adjustment, and surface processes from a joint inversion of satellite altimeter, gravity, and GPS data, *J. Geophys. Res*. *Earth Surf.*, 121, 182–200, doi:10.1002/2015JF003550.

Martin-Español, A., King, M. A., Zammit-Mangion, A., Andrews, S. B., Moore, P. & Bamber J. L. (2016b), An assessment of forward and inverse GIA solutions for Antarctica, *J. Geophys. Res. Solid Earth*, 121, 6947–6965, doi:10.1002/2016JB01315.

Moholdt, G., Nuth, C., Hagen, J. O., & Kohler, J. (2010). Recent elevation changes of Svalbard glaciers derived from ICESat laser altimetry. *Remote Sens. Environ.*, 114(11), 2756-2767.

Morelli, A., & Danesi, S. (2004). Seismological imaging of the Antarctic continental lithosphere: a review. *Global Planet. Change*, 42(1), 155-165.

Mouginot, J., Rignot, E., & Scheuchl, B. (2014). Sustained increase in ice discharge from the Amundsen Sea Embayment, West Antarctica, from 1973 to 2013. *Geophys. Res. Lett.*, 41(5), 1576-1584.

Nield, G. A., Whitehouse, P. L., King, M. A., Clarke, P. J., & Bentley, M. J. (2012). Increased ice loading in the Antarctic Peninsula since the 1850s and its effect on glacial isostatic adjustment. *Geophys. Res. Lett.*, 39(17).

Nield, G. A., Barletta, V. R., Bordoni, A., King, M. A., Whitehouse, P. L., Clarke, P. J., Domack, E., Scambos, T. A., Berthier, E. (2014). Rapid bedrock uplift in the Antarctic Peninsula explained by viscoelastic response to recent ice unloading. Earth Planet. Sci. Lett., 397, 32-41.

Peltier, W. R., & Andrews, J. T. (1976). Glacial-isostatic adjustment—I. The forward problem. Geophysical Journal International, 46(3), 605-646.

Peltier, W. R. (2004). Global glacial isostasy and the surface of the ice-age Earth: The ICE-5G (VM2) model and GRACE. *Annu. Rev. Earth Planet. Sci.*, 32, 111-149.

Priestley, K., & McKenzie, D. (2013). The relationship between shear wave velocity, temperature, attenuation and viscosity in the shallow part of the mantle. *Earth Planet. Sci. Lett.*, 381, 78-91.

Ranalli, G., & Murphy, D. C. (1987). Rheological stratification of the lithosphere. *Tectonophysics*, 132(4), 281-295.

Raymond, C. A., E. R. Ivins, M. B. Heflin and T. S. James, (2004). Quasi-continuous global positioning system measurements of glacial isostatic deformation in the northern Transantarctic Mountains. Glob. Plant. Change, 42, 295-303.

Retzlaff, R., and C. Bentley (1993), Timing of stagnation of Ice Stream C, West Antarctica, from short-pulse radar studies of buried surface crevasses, *J. Glaciol.*, 39(133), 533–561.

Rignot, E., Mouginot, J., Morlighem, M., Seroussi, H., & Scheuchl, B. (2014). Widespread, rapid grounding line retreat of Pine Island, Thwaites, Smith, and Kohler glaciers, West Antarctica, from 1992 to 2011. *Geophys. Res. Lett.*, 41(10), 3502-3509.

Riva, R. E., Gunter, B. C., Urban, T. J., Vermeersen, B. L., Lindenbergh, R. C., Helsen, M. M., . Bamber, J. L, van de Wal, R., van den Broeke, M. R. & Schutz, B. E. (2009). Glacial isostatic adjustment over Antarctica from combined ICESat and GRACE satellite data. *Earth Planet. Sci. Lett.*, 288(3), 516-523.

Sasgen, I., Martinec, Z., & Fleming, K. (2006). Wiener optimal filtering of GRACE data. *Stud Geophys Geod.*, 50(4), 499-508.

Sasgen, I., Dobslaw, H., Martinec, Z., & Thomas, M. (2010). Satellite gravimetry observation of Antarctic snow accumulation related to ENSO. *Earth Planet. Sci. Lett.*, 299(3), 352-358.

Sasgen, I., Konrad, H., Ivins, E. R., Van den Broeke, M. R., Bamber, J. L., Martinec, Z., & Klemann, V. (2013): Antarctic ice-mass balance 2003 to 2012: regional reanalysis of GRACE satellite gravimetry measurements with improved estimate of glacial-isostatic adjustment based on GPS uplift rates, The Cryosphere, 7, 1499-1512, doi:10.5194/tc-7-1499-2013.

Sasgen, I., Martín-Español, A., Horvath, A., Klemann, V., Petrie. E.J., Wouters, B., Horwath, M., Pail, R., Bamber, J.L., Clarke, P.J., Konrad, H. & Drinkwater, M. R., Joint inversion estimate of regional glacial isostatic adjustment in Antarctica considering a lateral varying Earth structure (ESA STSE Project REGINA), *Geophys. J. Int.*, 211(3), 1534-1553, doi:10.1093/gji/ggx368

Scambos, T., and C. Schuman (2016), Comment on 'Mass gains of the Antarctic ice sheet exceed losses' by H. J. Zwally and others, *J. Glaciol.*, 62, 599–603, doi:10.1017/jog.2016.59.

Schotman, H. H. A., Wu, P., & Vermeersen, L. L. A. (2008). Regional perturbations in a global background model of glacial isostasy. Physics of the Earth and Planetary Interiors, 171(1), 323-335.

Schroeder, D. M., Blankenship, D. D., Young, D. A., & Quartini, E. (2014). Evidence for elevated and spatially variable geothermal flux beneath the West Antarctic Ice Sheet. Proceedings of the National Academy of Sciences, 111(25), 9070-9072.

Shapiro, N. M., & Ritzwoller, M. H. (2004). Inferring surface heat flux distributions guided by a global seismic model: particular application to Antarctica. *Earth Planet. Sci. Lett.*, 223(1), 213-224.

Shepherd, A. (2012). A reconciled estimate of ice-sheet mass balance, Science, 338(6114), 1539-1539.

Sjöberg, L., Walyeldeen, H. & Horemuz, M. (2011). Estimation of Crustal Motions at the Permanent GPS Station SVEA, Antarctica from 2005 to 2009. *J. Geod. Sci*. 1(3): 215-220, doi:10.2478/v10156-010-0024-1.

Swenson, S., & Wahr, J. (2006). Post-processing removal of correlated errors in GRACE data. *Geophys. Res. Lett.*, 33(8), L08402.

Thomas, I. D., King, M. A., Bentley, M. J., Whitehouse, P. L., Penna, N. T., Williams, S. D. P., Riva, R. E. M., Lavallee, D. A., Clarke, P. J., King, E. C. & others (2011). Widespread low rates of Antarctic glacial isostatic adjustment revealed by GPS observations. *Geophys. Res. Lett.*, 38(22), L22302. doi: 10.1029/2011gl049277

van der Wal, W., Whitehouse, P. L., & Schrama, E. J. (2015). Effect of GIA models with 3D composite mantle viscosity on GRACE mass balance estimates for Antarctica. *Earth Planet. Sci. Lett.*, 414, 134-143.

van Ommen, T. D., Morgan, V., & Curran, M. A. (2004). Deglacial and holocene changes in accumulation at Law Dome, East Antarctica. Annals of Glaciology, 39(1), 359-365.

Wahr, J., Wingham, D., & Bentley, C. (2000). A method of combining ICESat and GRACE satellite data to constrain Antarctic mass balance. *J. Geophys. Res.*: *Solid Earth*, 105(B7), 16279-16294.

Wan, H., Giorgetta, M. A., Zängl, G., Restelli, M., Majewski, D., Bonaventura, L., Fröhlich, K., Reinert, D., Rípodas, P., Kornblueh, L., and Förstner, J. (2013), The ICON-1.2 hydrostatic atmospheric dynamical core on triangular grids – Part 1: Formulation and performance of the baseline version, *Geosci. Model Dev.*, 6, 735-763, doi:10.5194/gmd-6-735-2013, 2013.

Wessel, P., Smith, W. H. F., Scharroo,R, Luis, J. F. and Wobbe, F. Generic Mapping Tools: Improved version released, EOS Trans. AGU, 94, 409-410, 2013.

Williams, S. (2008). CATS: GPS coordinate time series analysis software. *GPS Solutions* 12(2): 147-153.

Whitehouse, P. L., Bentley, M. J., Milne, G. A., King, M. A., and Thomas, I. D. (2012): A new glacial isostatic adjustment model for Antarctica: calibrated and tested using observations of relative sea-level change and present-day uplift rates, *Geophys. J. Int.*, 190, 1464–1482, doi:10.1111/j.1365-246X.2012.05557.x.

Wolstencroft, M., King, M. A., Whitehouse, P. L., Bentley, M. J., Nield, G. A., King, E. C., McMillan, M., Shepherd, A., Barletta, V., Bordoni, A. & others (2015). Uplift rates from a new high-density GPS network in Palmer Land indicate significant late Holocene ice loss in the southwestern Weddell Sea. *Geophys. J. Int.*, 203(1), 737-754.

Wouters, B., Bonin, J. A., Chambers, D. P., Riva, R. E. M., Sasgen, I., & Wahr, J. (2014). GRACE, time-varying gravity, Earth system dynamics and climate change. *Rep. Prog. Phys.*, 77(11), 116801.

Wu, X., Heflin, M. B., Schotman, H., Vermeersen, B. L., Dong, D., Gross, R. S., Ivins, E. R., Moore, A. W. & Owen, S. E. (2010). Simultaneous estimation of global present-day water transport and glacial isostatic adjustment. *Nat. Geosci.*, 3(9), 642-646.